doi.org/10.26434/chemrxiv.7246859.v1

A Bifunctional Iron Nickel Catalyst for the Oxygen Evolution Reaction

fang song, Michael Busch, Benedikt Lassalle-Kaiser, Chia-Shuo Hsu, Elitsa Petkucheva, Michaël Bensimon, Hao Ming Chen, Clemence Corminboeuf, Xile Hu

Submitted date: 24/10/2018 • Posted date: 25/10/2018

Citation information: song, fang; Busch, Michael; Lassalle-Kaiser, Benedikt; Hsu, Chia-Shuo; Petkucheva, Elitsa; Bensimon, Michaël; et al. (2018): A Bifunctional Iron Nickel Catalyst for the Oxygen Evolution Reaction. ChemRxiv. Preprint.

The oxygen evolution reaction (OER) is a key process that enables the storage of renewable energies in the form of chemical fuels. Although numerous transition metal oxides have been explored as OER catalysts, the scaling relationship of the binding energies of various surface-bound intermediates imposes a limit on the maximum activity of these oxides. While previous computational studies have suggested bifunctional catalysts might be capable of overcoming this limit, stable and non-precious catalysts of this type remain elusive. Here, we describe a catalyst that exhibits activity significantly higher than current state-of-the-art catalysts that operate in alkaline solutions, including the benchmark nickel iron oxide. This new catalyst is both easy to prepare and stable for many hours. Operando X-ray absorption spectroscopic data reveal that the catalyst is made of nanoclusters of gamma-FeOOH covalently linked to the edge sites of a gamma-NiOOH support. According to density functional theory computations, this structure allows a reaction path involving iron as the oxygen evolving center and a nearby terrace O site on the gamma-NiOOH support oxide as a hydrogen acceptor. This bifunctional mechanism circumvents the aforementioned maximum activity limit associated with the scaling relationship and leads to superior OER activity.

File list (2)

A Bifunctional Iron Nickel Catalyst for the Oxygen Evolution Reaction

Fang Song,[1] Michael M. Busch,[2] Benedikt Lassalle-Kaiser,[3] Chia-Shuo Hsu,[4] Elitsa Petkucheva,[1,5] Michaël Bensimon,[6] Hao Ming Chen,[4,*] Clemence Corminboeuf,[2,*] and Xile Hu[1,*]

[1] Laboratory of Inorganic Synthesis and Catalysis, Institute of Chemical Sciences and Engineering, Ecole Polytechnique Fédérale de Lausanne (EPFL), EPFL-ISIC-LSCI, BCH 3305, Lausanne, CH 1015 Switzerland.

[2] Laboratory for Computational Molecular Design, Institute of Chemical Sciences and Engineering, and National Center for Computational Design and Discovery of Novel Materials (MARVEL), Ecole Polytechnique Fédérale de Lausanne (EPFL), Lausanne, CH 1015 Switzerland.

[3] Synchrotron SOLEIL, L'Orme des Merisiers, Saint-Aubin, 91191 Gif-sur-Yvette, France

[4] Department of Chemistry, National Taiwan University, Taipei 10617, Taiwan

[5] Department of PEM Hydrogen systems, Acad. E. Budevski Institute of Electrochemistry and Energy Systems (IEES), Acad. G. Bonchev Str. Bl.10 , Sofia 1113 Bulgaria.

[6] General Environmental Laboratory, Institute of Environmental Engineering, Ecole Polytechnique Fédérale de Lausanne (EPFL), Lausanne 1015, Switzerland.

*Correspondence to: haomingchen@ntu.edu.tw, clemence.corminboeuf@epfl.ch; xile.hu@epfl.ch;

Abstract: The oxygen evolution reaction (OER) is a key process that enables the storage of renewable energies in the form of chemical fuels. Although numerous transition metal oxides have been explored as OER catalysts, the scaling relationship of the binding energies of various surface-bound intermediates imposes a limit on the maximum activity of these oxides. While previous computational studies have suggested bifunctional catalysts might be capable of overcoming this limit, stable and non-precious catalysts of this type remain elusive. Here, we describe a catalyst that exhibits activity significantly higher than current state-of-the-art catalysts that operate in alkaline solutions, including the benchmark nickel iron oxide. This new catalyst is both easy to prepare and stable for many hours. Operando X-ray absorption spectroscopic data reveal that the catalyst is made of nanoclusters of γ-FeOOH covalently linked to the edge sites of a γ-NiOOH support. According to density functional theory computations, this structure allows a reaction path involving iron as the oxygen evolving center and a nearby terrace O site on the γ-NiOOH support oxide as a hydrogen acceptor. This bifunctional mechanism circumvents the aforementioned maximum activity limit associated with the scaling relationship and leads to superior OER activity.

Main text

The water splitting reaction provides a convenient process through which intermittent renewable energies are stored in the form of chemical fuels, namely hydrogen and oxygen[1]. Although numerous transition metal oxides have been explored as catalysts for the oxygen evolution reaction (OER, $2H_2O \rightarrow O_2 + 4H^+ + 4e^-$)[2,3], this reaction remains a bottleneck in the water splitting reaction. While only precious IrO_x, RuO_x, and their composites have sustained OER activity in acidic solutions, a number of non-precious metal oxides are reported to have higher activity than IrO_x[4-8] in alkaline solutions.

On metal oxides, the OER proceeds via multiple surface-bound intermediates including M-OH, M-OOH, and M=O (M denotes a metallic active site). A commonly proposed mechanism for OER in alkaline solutions consists of the following four steps[2,4,9-11]:

$$OH^- + M \rightarrow M\text{-}OH + e \quad (1)$$
$$M\text{-}OH + OH^- \rightarrow M{=}O + H_2O + e \quad (2)$$
$$M{=}O + OH^- \rightarrow M\text{-}OOH + e \quad (3)$$
$$M\text{-}OOH + OH^- \rightarrow O_2 + H_2O + M + e \quad (4)$$

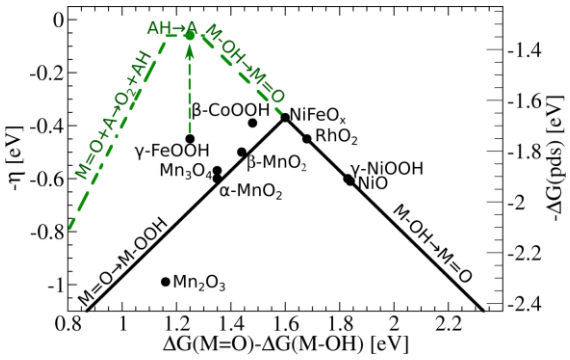

Figure 1 | Volcano plots assuming mono-nuclear (black) and bifunctional OER mechanisms (green). A denotes an arbitrary H acceptor site. γ-FeOOH has been computed in this work while all other oxides were taken from literature. Mn_3O_4, NiO, RhO_2[9]; β-CoOOH [12]; Mn_2O_3, α-MnO_2, β-MnO_2[13]; $NiFeO_x$, γ-NiOOH[10].

The potential determining step is either the formation of M=O (step 2) or the step forming the O-O bond by hydroxide attack of the M=O species (step 3) depending on their respective potentials (black slopes in Fig. 1). The adsorption energies of OH, O, and OOH are correlated. In particular, the difference in the surface adsorption energy of OH and OOH is, according to Density Functional Theory (DFT) computations, independent of the catalyst and approximately 3.2 eV[9,14]. Because of this scaling relationship, the minimal theoretical overpotential (η) for an oxide catalyst is about 0.4 V. According to computations[9,10,15], on catalysts like NiO, γ-NiOOH, and RhO_2, O binds too weakly which causes the formation of M=O to become potential determining and the overpotential increases beyond 0.4 V. For catalysts like Mn_3O_4, α-MnO_2, β-MnO_2, IrO_2, and β-CoOOH, O is too strongly bound and the formation of M=O occurs below 1.6 V[9,12,13]. The potential determining step is the O-O bond formation, which requires more than 1.6 V. The theoretical overpotential is again larger than 0.4 V. For $NiFeO_x$, both steps 2 and 3 occur at about 1.6 V, putting it near the top of a Sabatier-type Volcano-plot (Fig. 1)[10]. Thus, $NiFeO_x$ is predicted to be among the "most active" OER catalysts, far superior to NiOOH, CoO_x, and MnO_x. This prediction agrees well with experimental results[9,10,12,13]. To date, the scaling relationship has proven to govern the majority

of metal oxide catalysts, including all the known "most active" mixed oxide catalysts such as $NiFeO_x$, $CoFeO_x$, and FeCoW oxyhydroxide[15-17].

In order to overcome the performance limit of OER catalysts imposed by the scaling relationship, catalysts that operate by unconventional mechanisms need to be developed. Through DFT-based computational analysis, Rossmeisl and co-workers proposed that introducing proton acceptor-donor sites might lead to a bifunctional pathway for O-O bond formation, thereby circumventing the volcano limit in the OER[18-20]. Analogous bifunctional mechanisms have been reported for highly active catalysts in ammonium synthesis from nitrogen[21] and methanol synthesis from CO_2 [22]. For the OER, however, there is yet no experimental report of non-precious bifunctional catalysts that outperform the best conventional catalysts. Here, we describe a new OER catalyst that significantly surpasses the current performance limit of all known metal oxides in alkaline solutions, including the current state-of-the-art $NiFeO_x$ catalyst. This catalyst is stable and can be easily prepared from nickel foam (NF), a readily available and commonly used substrate in OER. Operando X-ray absorption spectroscopy reveals the unique structure of this catalyst consisting of nanoclusters of γ-FeOOH covalently linked to the edge sites of a γ-NiOOH support, which is formed in situ on NF. DFT computations suggest that this structure allows for a bifunctional mechanism facilitating the O-O bond formation, leading to exceptional catalytic activity.

NF is widely used as a 3-dimensional support for OER catalysts[15,23], but its intrinsic activity is modest (Fig. 2a). Since it has been shown that iron incorporation is required to enhance the OER activity of NiO_x-based catalysts[10,16,24,25], we hypothesized that the activity of NF might be increased in a similar way by iron incorporation. Fe ions were incorporated by potential cycling in commercial KOH, as it was previously shown that such a process led to the incorporation of Fe ions into NiO_x films[16]. Indeed when NF was subjected to 100 repetitive cyclic voltammetric (CV) scans from 1.21 to 1.54 V vs. RHE in a 1 M commercial KOH solution (with a Fe concentration of 0.18 mg L^{-1} according to measurements using Inductively Coupled Plasma Mass Spectrometry (ICP-MS)), a layer of Fe-containing nickel oxide (NiO_x-Fe) was formed. A NF-NiO_x-Fe electrode (loading of iron oxide: 4.3 μg cm^{-2}) exhibits much higher OER activity than NF (Fig. 2a). The as-received NF was then immersed into a solution containing 10 wt% hydrochloric acid (HCl) for 30 minutes, which resulted in a NF-AC (AC = acid cleaned) electrode with a rougher surface than NF according to the scanning electron microscopy images (Supplementary Fig. 1). After repetitive CV or linear sweep voltammetric (LSV) scans from 1.21 to 1.54 V vs. RHE in a 1 M commercial KOH solution, NF-AC-NiO_x-Fe electrodes were prepared. According to ICP-MS, the iron oxide loadings were in the range of 1.0-14.1 μg cm^{-2} depending on the preparation procedure (details are provided in Supplementary Information).

The NF-AC-NiO_x-Fe electrodes exhibit excellent OER activity (Fig. 2a and Supplementary Fig. 2a). To reach 10 mA cm^{-2}, a NF-AC-NiO_x-Fe electrode (loading of iron oxide: 14.1 μg cm^{-2}) requires an overpotential of 245 mV, lower than NF-NiO_x-Fe (266 mV) and NF (311 mV). The Tafel slopes are 34, 36, and 45 mV dec^{-1} for NF-AC-NiO_x-Fe, NF-NiO_x-Fe, and NF, respectively (Supplementary Fig. 3). The activity of the NF-AC-NiO_x-Fe electrode is stable: the overpotential for a current density of 10 mA cm^{-2} remained at 245 mV during an electrolysis of 18 hours (Fig. 2b). When NF-AC was subjected to 100 CV scans in a 1 M KOH solution that was stripped of Fe ions by sequestration with an excess of nickel hydroxides for 12 h (the Fe concentration is below the detection limit of ICP-MS after the treatment), the resulting Fe-free NF-AC-NiO_x exhibited much lower OER activity (Supplementary Fig. 4). Thus, Fe incorporation was essential for the high OER activity of the NF-AC-NiO_x-Fe and NF-NiO_x-Fe electrodes.

By using commercial KOH solution which contained only a trace amount of Fe ions, the maximum amount of Fe incorporation into NF-AC electrodes was limited to about 14 μg

cm^{-2}. Although this method of Fe incorporation seemed to be important for the optimal distribution of Fe active sites and the corresponding site-averaged activity (see below), the geometrically averaged activity might benefit from a higher loading of Fe. Such activity is relevant to practical applications, especially because Fe is cheap. To incorporate more Fe in NF-AC, we dipped the latter into a $FeCl_3$ solution (0.01 M) for 15 minutes and then dried it in an oven at 70 °C. The resulting electrode, NF-AC-FD (FD = Fe dipping), has hierarchical nanoporous structures at the surface (Supplementary Fig. 5). NF-AC-FD was subjected to 100 repetitive cyclic voltammetric (CV) scans from 1.21 to 1.53 V vs. RHE in a 1 M commercial KOH solution to yield the NF-AC-FD-NiO_x-Fe electrode. This electrode has much better net activity than NF-AC-NiO_x-Fe, reaching 10 mA cm^{-2} and 100 mA cm^{-2} at only 215 mV and 248 mV (Fig. 2a), respectively. The activity is stable for 36 h at least(Fig. 2b).

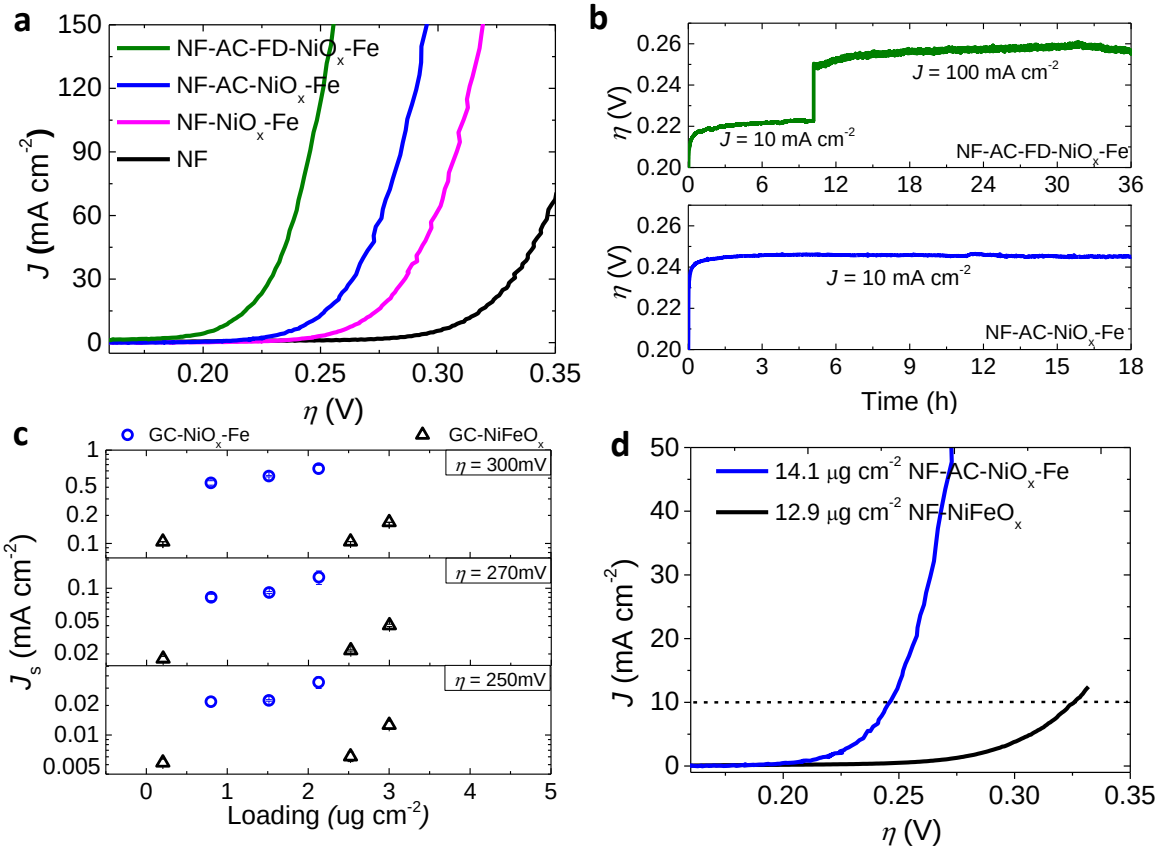

Figure 2 | Activity and stability of catalysts. a, Polarization curves of NF (black), NF-NiO_x-Fe (magenta), NF-AC-NiO_x-Fe (blue) and NF-AC-FD-NiO_x-Fe (green). Loadings of iron oxide in NF-NiO_x-Fe, NF-AC-NiO_x-Fe, and NF-AC-FD-NiO_x-Fe are 4.3, 14.1, and 68.0 μg cm^{-2}, respectively. Backward scan; Scan rate: 1 mV s^{-1}; IR corrected. **b,** Chronopotentiometric measurements of OER at 10 mA cm^{-2} for 18 h using NF-AC-NiO_x-Fe (bottom) as catalyst and at 10 mA cm^{-2} and 100 mA cm^{-2} for 36 h using NF-AC-FD-NiO_x-Fe (top) as catalyst. **c,** The J_s at different loadings of Fe_2O_3 for GC-NiO_x-Fe (blue spheres) and GC-$NiFeO_x$ (black triangles). **d**, Comparison of polarization curves between NF-AC-NiO_x-Fe and NF-$NiFeO_x$ at similar loading.

Table 1. **Comparison of TOFs and J_s of selected state-of-the-art OER catalysts in alkaline solutions.**[a]

Catalysts	Electrode	Overpotential				Reference
		270 mV		300 mV		
		TOF (s^{-1})	J_s (mA cm^{-2})	TOF (s^{-1})	J_s (mA cm^{-2})	
NF-AC-NiO_x-Fe	NF	0.78±0.27	0.041±0.018	3.4±1.1	0.18±0.08	This work
NF-AC-FD-NiOx-Fe	NF	0.82±0.13	0.051±0.008	n/a	n/a	This work
Au-NiOx-Fe	Au	0.73±0.23	0.17±0.03	3.5±1.3	0.81±0.17	This work
GC-NiOx-Fe	GC	0.48±0.10	0.10±0.03	2.5±0.44	0.54±0.09	This work
NF-$NiFeO_x$ [b]	NF	0.06±0.02	0.012±0.002	0.33±0.06	0.05±0.01	This work
GC-$NiFeO_x$ [b]	GC	0.10±0.02	0.03±0.01	0.44±0.05	0.13±0.04	This work
$NiFeO_x$ [c]	GC/Au	0.072±0.02 [e]	0.011 [e]	0.52±0.16	0.084	[8,16]
$NiFeO_x$	Au	n/a	0.015±0.010 [e]	n/a	0.11±0.07 [e]	[7]
NiFe LDH	GC	0.036	n/a	0.21	n/a	[6]
G-FeCoW	GC	n/a	n/a	0.93	n/a	[15]
IrO_2 [d]	Au	~0.002 [e]	0.004 [e]	~0.01	0.02	[5,7]

[a] For multiple samples, the averaged values with standard deviations are given. For NF-AC-NiO_x-Fe, Au-NiO_x-Fe, and GC-NiO_x-Fe, each sample is measured 2-3 times and the raw data are shown in Supplementary Table 1-3. For all iron-containing samples except G-FeCoW, iron is assumed as the active species; for G-FeCoW, Co is taken as the active species. n/a is the abbreviation for the phrase of not available due to lack of data or influence by mass transfer. [b] $NiFeO_x$ was prepared according to the method reported in literature [16] (Supplementary Methods). Each sample is measured 2 times and the raw data are shown in Supplementary Table 4. [c] TOFs were taken from the samples on GC reported in literature[16]. J_s are taken from the continuously deposited film on Au reported in literature[8] (calculation of J_s see in Supplementary Methods). [d] TOFs are taken from literature[5] and J_s are taken from literature[7]. [e] TOFs and J_s at these potentials are extrapolated using the reported Tafel slopes (~35 mV dec^{-1} for $NiFeO_x$, ~40 mV dec^{-1} for IrO_2).

Three figures of merits including turnover frequency (TOF), surface area averaged specific activity, and overpotential for 10 mA cm^{-2}, are commonly used to compare OER catalysts[7]. The first two parameters focus on the intrinsic activity of catalysts, while the third one is oriented towards device performance. These three parameters were determined for the catalyst reported here and compared to the best performing OER catalysts in alkaline solutions (Table 1, Supplementary Table 5-7). It appears that this catalyst outperforms all other catalysts for at least 2 of these parameters and competes very well for all of them.

As electrochemical, spectroscopic and computational data (see below) indicate that the active site of our catalyst is Fe, the apparent TOFs of the NF-AC-NiO_x-Fe electrodes were calculated according to the total amount of Fe ions, as determined by ICP-MS (Supplementary Fig 6; Supplementary Tables 1; Supplementary Methods). TOFs were calculated for 10 different electrodes with a Fe (Fe oxide) loading in the range of 1.4 to 14.1 μg cm^{-2}, and were found to be similar. Table 1 compares the averaged TOFs of NF-AC-NiO_x-Fe with several state-of-the-art catalysts, and Supplementary Table 5 lists the comparison with an extended number of known catalysts. All TOFs were calculated according to the total amounts of active metal ions. NF-AC-NiO_x-Fe and NF-AC-FD-NiO_x-Fe have similar TOFs. Their TOFs are the highest among all solid-state catalysts reported to date. With an average TOF of 0.78 s^{-1} at η = 270 mV, NF-AC-NiO_x-Fe is about an order of magnitude more active than state-of-the-art $NiFeO_x$ and NiFe LDH catalysts[6,16] and more than 200 times higher than IrO_2. Recently a gelled FeCoW oxyhydroxide (G-FeCoW) was reported to be the hitherto most active OER catalyst in alkaline solutions[15]. NF-AC-NiO_x-Fe has a TOF 3.6 times higher than G-FeCoW. To alleviate the uncertainty using literature values when comparing TOFs, direct comparison of NF-AC-NiO_x-Fe with $NiFeO_x$ deposited on NF was conducted (Supplementary Table 4 and Table 5). The TOFs of NF-AC-NiO_x-Fe are again 10-13 times higher than those of NF-$NiFeO_x$.

In the above calculation of TOFs for NF-AC-NiO_x-Fe and NF-AC-FD-NiO_x-Fe, the NiO_x component was treated as a support for the active Fe centers. For this assumption to be valid, the TOFs should be independent of the quantity of NiO_x. To verify this assumption, thin layers of NiO_x were first electrodeposited on Au and glassy carbon (GC) electrodes, followed by iron-incorporation using the same method as for the synthesis of NF-AC-NiO_x-Fe. On these two electrodes, the quantity of NiO_x could be varied and measured. The activity of the resulting catalysts, Au-NiO_x-Fe and GC-NiO_x-Fe, were measured by LSV (Supplementary Fig. 7). Notwithstanding a small difference, both Au-NiO_x-Fe and GC-NiO_x-Fe exhibit activities and TOFs (Table 1, Supplementary Fig. 7 and Supplementary Tables 1-3) similar to NF-AC-NiO_x-Fe. The small difference is likely due to the electrical contact between the NiO_x film and the electrodes rather than the intrinsic activity of the catalyst. The TOFs of Au-NiO_x-Fe and GC-NiO_x-Fe are largely independent of the quantity of NiO_x (Supplementary Fig. 8). These data validate the treatment of NiO_x as a support in the calculation of TOFs of our catalysts and show that it outperforms all alkaline OER catalysts reported so far.

The specific activity (J_s), which is the current density averaged by the electrochemical surface area, is a parameter that is complementary to TOF in evaluating the intrinsic activity of electrocatalysts[7]. To make a direct comparison, the specific activities of our NiO_x-Fe catalyst and $NiFeO_x$ deposited on the same supports (NF and GC) were measured (Supplementary Methods). It was previously reported that $NiFeO_x$ had the highest specific activity among various transition metal oxides[7]. On both electrodes, our catalyst has 3-4 times higher specific activity than $NiFeO_x$ (Fig. 2c, Table 1 and Supplementary Table 6). The specific activity on GC is higher than on NF for both catalysts because electrochemical surface areas correspond only to those of the catalysts due to the GC's flat surface, while on NF the areas correspond to those of the porous NF electrodes. The values on GC are therefore representative of the true activity of the catalysts. For the $NiFeO_x$ catalyst, our value is similar to those determined in the literature[7,8], confirming that the $NiFeO_x$ catalyst used in the direct comparison exhibits the same activity as the state-of-the-art samples. The intrinsic activity of the bifunctional NiO_x-Fe catalysts is therefore superior to all known catalysts for which an intrinsic activity have been reported.

Another important parameter of catalytic activity is the overpotential for a given current density, e.g., 10 mA cm^{-2} (Supplementary Table 7). In direct comparison and at similar loadings, the present NiO_x-Fe catalyst has overpotentials of about 74-80 mV lower than $NiFeO_x$ (Fig. 2d, and Supplementary Fig. 9). A striking improvement of more than 160 mV in overpotential is

obtained when comparing NF-AC-NiO_x-Fe with IrO_2, the benchmark noble metal catalyst, at a similar loading. A small number of high-surface-area electrodes coated with a large amount of catalysts are reported to have overpotentials close to 200 mV for 10 mA cm^{-2}, making them interesting for device performance (Supplementary Table 8)[15,23,26]. With an overpotential of only 215 mV, a stable activity, and an easy and economical preparation from earth abundant components, the NF-AC-FD-NiO_x-Fe electrode described above is also very competitive in this category.

The NiO_x-Fe catalyst was subjected to a variety of characterization methods. X-ray photoelectron spectroscopy (XPS) data are consistent with the presence of iron oxide on the surface of the electrode (Supplementary Fig. 10)[27]. In the Raman spectra, the peaks corresponding to γ-NiOOH, initially absent in the catalyst before OER, emerged after subjecting the catalyst to OER conditions (Supplementary Fig. 11). This lamellar structure has already been shown to be the active phase in nickel containing OER catalysts under oxidative potentials.[28] No peak from an iron oxide species was, however, observed in the Raman spectra, probably because of the low iron concentration. To obtain further structural information on the catalyst, X-ray absorption spectroscopy (XAS) was applied, both on the post-catalytic material and under operating conditions.

Figure 3a shows the Fe K-edge X-ray absorption near edge spectra (XANES) of NF-AC-NiO_x-Fe, together with iron oxide references[29]. The oxidation state of as-prepared NF-AC-NiO_x-Fe is close to the value of +3, since the main absorption edge position coincides with that of γ-Fe(3+)OOH. Spinel iron oxides (maghemite and magnetite) and hematite contain both octahedral and tetrahedral sites. Tetrahedral iron sites have a well-defined signature in Fe K-pre-edge with an intense peak at low energies (ca. 7114 eV)[30,31]. From the pre-edge intensity and position (inset of Fig. 3a), the tetrahedrally coordinated Fe ions can therefore be ruled out. This result is confirmed by Extended X-ray Absorption Fine Structure (EXAFS) spectra at the Fe K-edge (as depicted in Fig. 3b), which further describes the local geometry of Fe. The first peak at apparent distances 1.5 Å and the second and third peaks at 2.5 and 3.1 Å, are attributed to the single scattering path of the closest oxygen (that is, Fe-O) and the second/third neighboring iron metals (that is, Fe-Fe) surrounding the absorbing Fe ions[32,33], respectively. These results clearly reveal the Fe-Fe bonds with octahedrally coordinated Fe ions in NF-AC-NiO_x-Fe, which are more similar to those of γ-FeOOH or NiFe-LDH and Fe-doped γ-NiOOH[24], as opposed to hematite or spinel structures. Most interestingly, a new peak (Fe-$Ni_{outside}$) was observed at 3.98 Å (Fig. 3b, Supplementary Table 9 and Supplementary Fig. 12 - Fig. 14); this value is significantly larger than those of both Fe-$Fe_{(Td)}$ and Fe-$Fe_{(Oh)}$ in hematite or spinel structures, as well as that of Fe-Ni in NiFe LDH (~3.1 Å), indicating that there is a Fe-Ni path with a specific long distance in NF-AC-NiO_x-Fe (~4.0 Å). This specific path is attributed to an interfacial interaction between the octahedrally oxygen-coordinated Fe and the underlying closest NiO_x through an oxygen bridge. Notably, the coordination number (CN) of Fe-Fe is remarkably smaller than those of Lepidocrocite (γ-FeOOH) or NiFe-LDH. This result reveals small size clusters (~1-2 nm), where the Fe ions at the edges have fewer Fe-Fe interactions than in the center (Supplementary Table 9 and Supplementary Fig. 13 - 14), thus decreasing the overall mean Fe-Fe coordination numbers. Accordingly, the NF-AC-NiO_x-Fe catalyst can be described as discrete nanoclusters of γ-FeOOH covalently linked to the NiO_x support (with a γ-NiOOH structure under OER, see Raman data above and XAS data below) via bridging oxygens (Fig. 3c). The lack of Fe-Ni path at about 3.1 Å as found in NiFe LDH (Supplementary Fig. 14) indicates that the FeO_6 octahedron and the NiO_6 octahedron are not edge-sharing as in NiFe LDH, but corner-sharing which leads to a Ni-O-Fe distance of about 4 Å. Therefore, the interface between the FeOOH clusters and the γ-NiOOH support occurs at the edge, but not terrace, sites of γ-NiOOH (Fig. 3c).

In-situ X-ray absorption spectroscopy was employed to reveal the structural evolution of the catalyst during OER (Fig. 3d, Table 2 and Supplementary Table 10)[34,35]. In order to collect Ni K-edge data, the catalysts deposited on Au-coated FTO (Au-NiO_x-Fe) were used instead of NF-AC-NiO_x-Fe due to the strong background Ni signal from NF. The Fe K-edge data of Au-NiO_x-Fe are similar to those of NF-AC-NiO_x-Fe, confirming the similar nature of catalysts on both supports. Prior to OER (when no bias or η = 0.22 V are applied), slight decreases in apparent distance are observed compared to the dry sample. These changes might be attributed to a specific interaction with the electrolyte. Once the applied voltage is further increased above η = 0.27 V, the apparent distance of Fe-Fe path is reduced by approximately 0.15 Å. This decrease in Fe-Fe path is due to the oxidation of Fe, as observed before in other systems[24,33]. Likewise, *in-situ* Ni K-edge XAS (Fig. 3d, Supplementary Fig. 15 and Supplementary Table 10) shows that the apparent distances of the Ni-Ni path is reduced by about 0.24-0.27 Å under OER potentials, indicating the oxidation of Ni ions. The potential dependent edge energies (Supplementary Fig. 16) indicate the transformation of the NiO_x support from α-$Ni(OH)_2$ to γ-NiOOH under OER conditions[24,28], in agreement with the result of the Raman study (see above).

The distance of Fe-$Ni_{outside}$ path changes dramatically, from 3.98 Å in the dry sample to 3.80 Å at no bias and η = 0.22 V to 3.34 Å at η = 0.27 V and further to 3.21 Å at η = 0.37 V. This result indicates strong structural changes at the interface of the γ-FeOOH clusters and the γ-NiOOH support. From the dry sample to the catalyst at the beginning of OER (η = 0.27 V), the structural change can be accounted for by considering a 52° tilt of the FeO_6 octahedron relative to the NiO_6 octahedron (Fig 3c). A further 3.6° tilt of the FeO_6 octahedron can account for the structural change from η = 0.27 V to η = 0.37 V. While the more than 50° tilt is significant, it seems feasible since the FeO_6 octahedrons in pure γ-FeOOH are tilted at about 23° degree one over the other (Supplementary Fig. 17). Notably, this significant structural change only occurs on NF-AC-NiO_x-Fe catalyst. The NiFe LDH reference sample, which is considered as the active form of $NiFeO_x$, exhibits no such structural changes according to *operando* XAS (Supplementary Fig. 18). This comparison further underscores the unique nature of the present NF-AC-NiO_x-Fe catalyst relative to $NiFeO_x$ and the peculiar role of the interaction between the NiOOH support and the discrete FeOOH clusters.

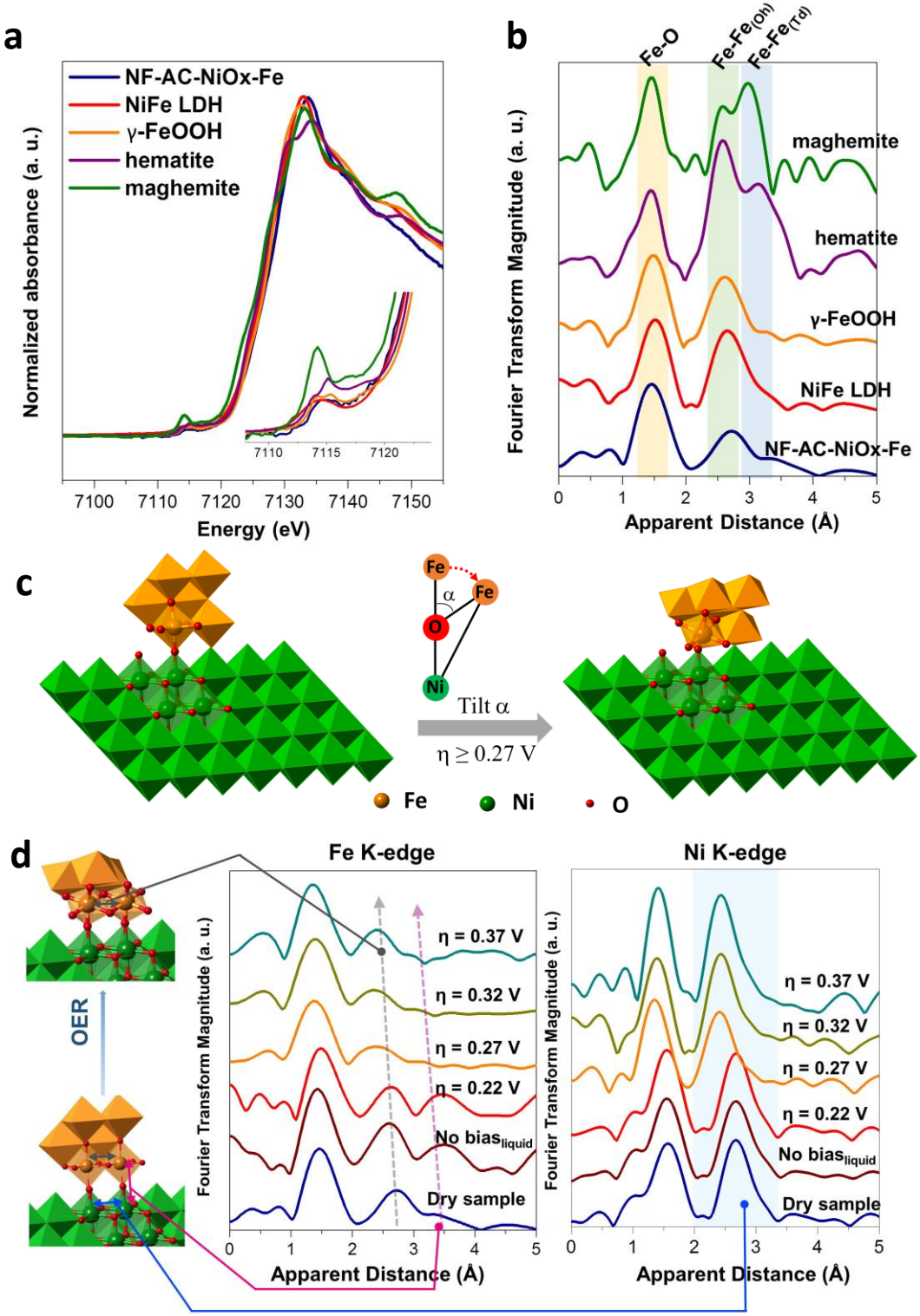

Figure 3 | *in-situ* X-ray absorption spectroscopy. **a,** XANES spectra, inset shows the pre-edge features of all spectra. **b**, Fourier transform of Fe K-edge EXAFS spectra for NF-AC-NiO_x-Fe and the corresponding references. **c**, Proposed model of γ-FeOOH onto NiOOH surface with geometric tilt. Inset shows the illustrative side view of the tilt (α is the tilt degree). **d,** *in-situ* FT-EXAFS spectra of Fe K-edge and Ni K-edge for Au-NiO_x-Fe during OER.

Table 2 | Structural parameters of Au-NiO_x-Fe sample extracted from *in-situ* Fe K-edge EXAFS refinement during OER.

condition	path	R (Å)	CN	ΔE (eV)	σ^2 (Å^2)	R-value (%)
	Fe-O	1.98(1)	4.8(2)	1.4(8)	0.0095(2)	0.798
Dry sample	**Fe-Fe**	3.06(2)	2.3(2)	1.3(6)	0.0071(1)	
	Fe-Ni$_{outside}$	3.98(4)	3.6(4)	3.2(7)	0.0080(6)	
	Fe-O	1.93(1)	5.3(3)	-1.7(3)	0.0023(2)	4.915
No bias	**Fe-Fe**	2.97(1)	4.5(5)	-7.3(4)	0.0055(3)	
	Fe-Ni$_{outside}$	3.83(2)	4.3(9)	1.2(9)	0.0058(5)	
	Fe-O	1.98(4)	5.9(3)	4.8(3)	0.0054(1)	5.906
η = 0.22	**Fe-Fe**	3.03(5)	4.0(8)	-1.6(5)	0.0073(2)	
	Fe-Ni$_{outside}$	3.80(7)	4.2(9)	-2.4(7)	0.0049(3)	
	Fe-O	1.91(1)	4.3(4)	-4.0(1)	0.0103(1)	3.800
η = 0.27	**Fe-Fe**	2.87(3)	2.3(3)	-4.4(1)	0.0120(4)	
	Fe-Ni$_{outside}$	3.34(4)	2.1(7)	-1.6(3)	0.0138(9)	
	Fe-O	1.93(1)	4.9(1)	-1.7(3)	0.0103(2)	1.907
η = 0.32	**Fe-Fe**	2.88(2)	2.3(6)	-2.9(3)	0.0108(4)	
	Fe-Ni$_{outside}$	3.22(6)	2.2(9)	-3.2(5)	0.0123(7)	
	Fe-O	1.91(1)	4.7(4)	-2.9(8)	0.0103(1)	11.580
η = 0.37	**Fe-Fe**	2.86(2)	3.1(2)	2.7(7)	0.0118(1)	
	Fe-Ni$_{outside}$	3.21(5)	1.9(7)	1.0(1)	0.0135(4)	

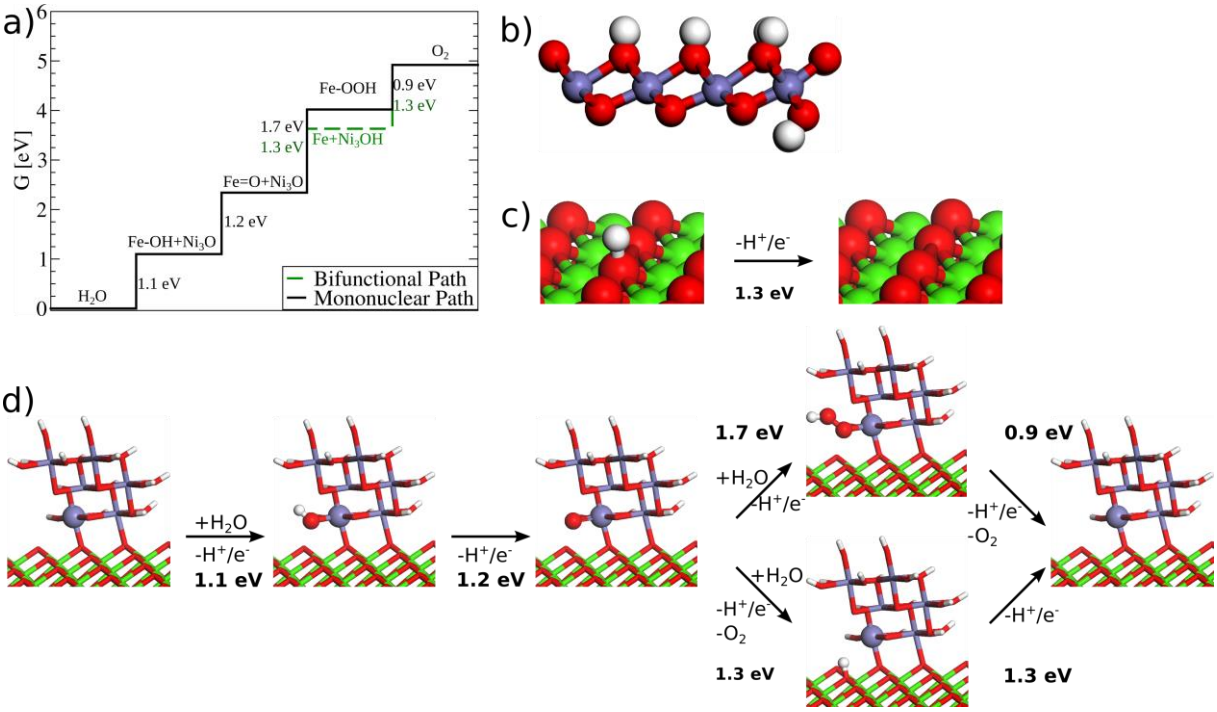

Figure 4 | DFT computations. a, Free energy diagram comparing the electrochemical potentials of water oxidation at γ-FeOOH proceeding through a mono-nuclear mechanism (black solid line) and a bifunctional mechanism with Ni_3-O sites acting as hydrogen acceptor (green dashed line). **b,** Schematic picture of the γ-FeOOH model. Color code: violet: Fe; red: O; grey: H. **c,** Ni_3-O hydrogen acceptor site at γ-NiOOH; Color code: Green: Ni; red: O; grey: H. **d,** Schematic representation of the OER reaction mechanism. Upper path: Mono-nuclear mechanism; lower path: Bifunctional mechanism. Color code: violet: Fe; green: Ni; red: O; grey: H.

The DFT computations shown in Figs. 1 and 4 assist in understanding how NF-AC-NiO_x-Fe can significantly outperform the state of the art $NiFeO_x$ catalyst. Here, a generic isolated γ-FeOOH was constructed. This model contains the key features of the active catalyst, *i.e.*, the brucite type structure and the octahedral coordination by six oxygen ligands (Fig. 4b). Computationally, this model has the advantage of representing potentially active Fe sites while avoiding complications resulting from interfacing the cluster with the γ-NiOOH support. As shown in Fig. 1, γ-FeOOH binds O too strongly and is placed on the strong binding side of the Sabatier volcano (Fig. 1). The formation of Fe=O has an equilibrium potential of only about 1.2 V. The potential determining step is the hydroxide attack on M=O, which has a potential of 1.7 V and results in a theoretical overpotential of 0.5 V (Fig. 4a). Thus, γ-FeOOH alone is only a modest catalyst. However, if the O-O bond forming step on γ-FeOOH can proceed through an alternative pathway, such as a bifunctional mechanism that avoids the potential limiting formation of M-OOH, the overpotential can be reduced[18]. The bifunctional mechanism assumes the direct formation of O_2 through a nucleophilic attack of OH^- coupled with a concerted H transfer to an adjacent acceptor site, A[18,19]:

$$M{=}O + OH^- + A \rightarrow M + O_2 + A\text{-}H + e \quad (5)$$

As the Fe ions in NF-AC-NiO_x-Fe are located on the edges of the γ-NiOOH support, we explored the H transfer to various nearby sites on γ-NiOOH as potential hydrogen acceptors. It was found that an Ni_3O site at a terrace plane of γ-NiOOH was a suitable hydrogen acceptor, with a potential of 1.3 V for $Ni_3O + H^+ + e^-$ to Ni_3OH (Fig. 4c). Such a site is abundantly present at the proximity of the Fe center (Fig. 4d). Incorporation of the Ni_3O hydrogen acceptor completely alters the energy landscape of the OER on γ-FeOOH (Fig. 4a and 4d). The O-O bond forming step now only has a potential of about 1.3 V, resulting in a theoretical overpotential of only 0.1 V. This bifunctional catalysis avoids the high-energy OOH intermediate and introduces two new slopes for a revisited Volcano plot (green curves in Fig. 1; see also Supplementary Fig. 19). The left slope represents a region where the O-O bond formation through a bifunctional mechanism determines the overpotential. A narrow plateau is found at the top of this Volcano plot, where the formation energy of M=O ranges from 1.1 to 1.3 eV. At this plateau the overpotential is determined by the recovery of the H acceptor site and the theoretical overpotential is at its minimum value of 0.1 V. The γ-FeOOH-Ni_3O bifunctional catalyst, which is proposed to be the active component of NF-AC-NiO_x-Fe, sits exactly at the top of the "bifunctional Volcano" and represents a new benchmark for metal oxide OER catalysts.

According to computations, the availability of γ-FeOOH sites, with an equilibrium potential of about 1.2 V for the formation of Fe=O, is a pre-requisite for the proposed bifunctional catalysis. In $NiFeO_x$, the Fe ions are incorporated into an extended lattice of γ-NiOOH. The resulting structural and electronic change shifts the Fe=O formation potential to

about 1.6 V[24] and as a consequence, the theoretical overpotential is 0.4 V with or without a suitable hydrogen acceptor.

In summary, an oxygen evolution catalyst based on earth abundant elements with an "off the scale" activity in alkaline solutions has been discovered. This catalyst not only significantly out-competes the most active current state-of-the-art $NiFeO_x$ catalyst, but it is also easily prepared and exhibits long-term stability. Applications can be envisioned for both alkaline electrolysers and photoelectrochemical water splitting devices, which often employ thin layers of nickel oxide as catalysts, heterojunction, or protection layers[36-40]. The experimental demonstration that bifunctional catalysis in the OER can lead to activity superior to the best conventional catalysts showcases its potential. A further implication of this work is that other bifunctional systems comprised of an active site with an equilibrium potential close to 1.23 V for the formation of M=O and a support with an equilibrium potential close to -1.23 V for hydrogen addition might also exhibit superior OER activity. Thus, this work should inspire numerous follow-up studies employing bifunctional catalysis as a new design strategy, leading to the next generation of OER catalysts that perform beyond the Volcano limits.

REFERENCES AND NOTES

1 Lewis, N. S. & Nocera, D. G. Powering the planet: Chemical challenges in solar energy utilization. *Proc. Natl. Acad. Sci. USA* **103**, 15729-15735 (2006).

2 Dau, H. *et al.* The mechanism of water oxidation: from electrolysis via homogeneous to biological catalysis. *ChemCatChem* **2**, 724-761 (2010).

3 Han, L., Dong, S. & Wang, E. Transition-metal (Co, Ni, and Fe)-based electrocatalysts for the water oxidation reaction. *Adv. Mater.* **28**, 9266-9291 (2016).

4 Suntivich, J., May, K. J., Gasteiger, H. A., Goodenough, J. B. & Shao-Horn, Y. A perovskite oxide optimized for oxygen evolution catalysis from molecular orbital principles. *Science* **334**, 1383-1385 (2011).

5 Trotochaud, L., Ranney, J. K., Williams, K. N. & Boettcher, S. W. Solution-cast metal oxide thin film electrocatalysts for oxygen evolution. *J. Am. Chem. Soc.* **134**, 17253-17261 (2012).

6 Song, F. & Hu, X. Exfoliation of layered double hydroxides for enhanced oxygen evolution catalysis. *Nat. Commun.* **5**, 4477 (2014).

7 McCrory, C. C. L., Jung, S. H., Peters, J. C. & Jaramillo, T. F. Benchmarking heterogeneous electrocatalysts for the oxygen evolution reaction. *J. Am. Chem. Soc.* **135**, 16977-16987 (2013).

8 Batchellor, A. S. & Boettcher, S. W. Pulse-electrodeposited Ni-Fe (oxy)hydroxide oxygen evolution electrocatalysts with high geometric and intrinsic activities at large mass loadings. *Acs Catal.* **5**, 6680-6689 (2015).

9 Man, I. C. *et al.* Universality in oxygen evolution electrocatalysis on oxide surfaces. *ChemCatChem* **3**, 1159-1165 (2011).

10 Diaz-Morales, O., Ledezma-Yanez, I., Koper, M. T. M. & Calle-Vallejo, F. Guidelines for the rational design of Ni-based double hydroxide electrocatalysts for the oxygen evolution reaction. *Acs Catal.* **5**, 5380-5387 (2015).

11 Rossmeisl, J., Logadottir, A. & Norskov, J. K. Electrolysis of water on (oxidized) metal surfaces. *Chem. Phys.* **319**, 178-184 (2005).

12 Bajdich, M., Garcia-Mota, M., Vojvodic, A., Norskov, J. K. & Bell, A. T. Theoretical investigation of the activity of cobalt oxides for the electrochemical oxidation of water. *J. Am. Chem. Soc.* **135**, 13521-13530 (2013).

13 Lehtimaki, M. *et al.* Targeted design of alpha-MnO_2 based catalysts for oxygen reduction. *Electrochim. Acta* **191**, 452-461 (2016).

14 Koper, M. T. M. Thermodynamic theory of multi-electron transfer reactions: Implications for electrocatalysis. *J. Electroanal. Chem.* **660**, 254-260 (2011).

15 Zhang, B. *et al.* Homogeneously dispersed multimetal oxygen-evolving catalysts. *Science* **352**, 333-337 (2016).

16 Trotochaud, L., Young, S. L., Ranney, J. K. & Boettcher, S. W. Nickel-iron oxyhydroxide oxygen-evolution electrocatalysts: The role of intentional and incidental iron incorporation. *J. Am. Chem. Soc.* **136**, 6744-6753 (2014).

17 Morales-Guio, C. G., Liardet, L. & Hu, X. Oxidatively electrodeposited thin-film transition metal (oxy)hydroxides as oxygen evolution catalysts. *J. Am. Chem. Soc.* **138**, 8946–8957 (2016).

18 Busch, M. *et al.* Beyond the top of the volcano? – A unified approach to electrocatalytic oxygen reduction and oxygen evolution. *Nano Energy* **29**, 126-135 (2016).

19 Halck, N. B., Petrykin, V., Krtil, P. & Rossmeisl, J. Beyond the volcano limitations in electrocatalysis - oxygen evolution reaction. *Phys. Chem. Chem. Phys.* **16**, 13682-13688 (2014).

20 Frydendal, R. *et al.* Enhancing activity for the oxygen evolution reaction: The beneficial interaction of gold with manganese and cobalt oxides. *ChemCatChem* **7**, 149-154 (2015).

21 Wang, P. K. *et al.* Breaking scaling relations to achieve low-temperature ammonia synthesis through LiH-mediated nitrogen transfer and hydrogenation. *Nat. Chem.* **9**, 64-70 (2017).

22 Graciani, J. *et al.* Highly active copper-ceria and copper-ceria-titania catalysts for methanol synthesis from CO_2. *Science* **345**, 546-550 (2014).

23 Luo, J. S. *et al.* Water photolysis at 12.3% efficiency via perovskite photovoltaics and Earth-abundant catalysts. *Science* **345**, 1593-1596 (2014).

24 Friebel, D. *et al.* Identification of highly active Fe sites in (Ni,Fe)OOH for electrocatalytic water splitting. *J. Am. Chem. Soc.* **137**, 1305-1313 (2015).
25 Corrigan, D. A. The catalysis of the oxygen evolution reaction by iron impurities in thin-film nickel-oxide electrodes. *J. Electrochem. Soc.* **134**, 377-384 (1987).
26 Zhou, H. Q. *et al.* Highly active catalyst derived from a 3D foam of $Fe(PO_3)_2/Ni_2P$ for extremely efficient water oxidation. *Proc. Natl. Acad. Sci. USA* **114**, 5607-5611 (2017).
27 Biesinger, M. C. *et al.* Resolving surface chemical states in XPS analysis of first row transition metals, oxides and hydroxides: Cr, Mn, Fe, Co and Ni. *Appl. Surf. Sci.* **257**, 2717-2730 (2011).
28 Bediako, D. K. *et al.* Structure-activity correlations in a nickel-borate oxygen evolution catalyst. *J. Am. Chem. Soc.* **134**, 6801-6809 (2012).
29 Monnier, J. *et al.* XAS and XRD in situ characterisation of reduction and reoxidation processes of iron corrosion products involved in atmospheric corrosion. *Corros. Sci.* **78**, 293-303 (2014).
30 Wilke, M., Farges, F., Petit, P.-E., Brown, G. E. & Martin, F. Oxidation state and coordination of Fe in minerals: An Fe K-XANES spectroscopic study. *Am. Min.* **86**, 714-730 (2001).
31 Westre, T. E. *et al.* A multiplet analysis of Fe K-edge 1s→3d pre-edge features of iron complexes. *J. Am. Chem. Soc.* **119**, 6297-6314 (1997).
32 Tung, C. W. *et al.* Reversible adapting layer produces robust single-crystal electrocatalyst for oxygen evolution. *Nat. Commun.* **6**, 8106 (2015).
33 Wang, H. Y. *et al.* In Operando identification of geometrical-site-dependent water oxidation activity of spinel Co_3O_4. *J. Am. Chem. Soc.* **138**, 36-39 (2016).
34 Suen, N. T. *et al.* Electrocatalysis for the oxygen evolution reaction: recent development and future perspectives. *Chem. Soc. Rev.* **46**, 337-365 (2017).
35 Lassalle-Kaiser, B., Gul, S., Kern, J., Yachandra, V. K. & Yano, J. In situ/Operando studies of electrocatalysts using hard X-ray spectroscopy. *J. Electron. Spectrosc. Relat. Phenom.* **221**, 18-27 (2017).
36 Zeng, K. & Zhang, D. K. Recent progress in alkaline water electrolysis for hydrogen production and applications. *Prog. Energ. Combust.* **36**, 307-326 (2010).
37 Kenney, M. J. *et al.* High-performance silicon photoanodes passivated with ultrathin nickel films for water oxidation. *Science* **342**, 836-840 (2013).
38 Hu, S. *et al.* Amorphous TiO_2 coatings stabilize Si, GaAs, and GaP photoanodes for efficient water oxidation. *Science* **344**, 1005-1009 (2014).
39 Kim, T. W. & Choi, K. S. Nanoporous BiVO4 photoanodes with dual-layer oxygen evolution catalysts for solar water splitting. *Science* **343**, 990-994 (2014).
40 Sun, K. *et al.* S Stable solar-driven oxidation of water by semiconducting photoanodes protected by transparent catalytic nickel oxide films. *Proc. Natl. Acad. Sci. USA* **112**, 3612-3617 (2015).

ACKNOWLEDGMENTS

This work is supported by the EPFL, the European Research Council (no.681292), the Zeno Karl Schindler Foundation, and The National Center of Competence in Research (NCCR) "Materials' Revolution: Computational Design and Discovery of Novel Materials (MARVEL)" of the Swiss National Science Foundation (SNSF). We also acknowledge support from the Ministry of Science and Technology, Taiwan (Contracts No. MOST 106-2119-M-002-031). Dr. Solenn Reguer, beamline scientist on the DIFFABS beamline at the SOLEIL Synchrotron is acknowledged for providing XAS spectra of reference samples. We thank Lucas-Alexandre Stern (EPFL) for discussion in synthesis, the Interdisciplinary Center for Electron Microscopy at EPFL for assistance in electron microscopic measurements, and the Material Characterization Platform at EPFL for assistance in Raman spectroscopic measurements. A

European priority patent application (no. 16189000.9) titled “Method of synthesis of an electrode for use as a catalyst of oxygen evolution reaction” was filed by EPFL with X.L. Hu, F. Song, and E. Petkucheva as inventors.

Author contributions

X.L.H and F.S. designed the experiments. C.C., X.L.H., and M.M.B designed the computations. F.S performed the majority of the synthesis, characterization, and electrochemical tests. M.M.B made the DFT computations. B.L-K and CSH measured the ex-situ X-ray absorption data. C.S.H performed the in-situ X-ray absorption experiments. E.P made supplementary electrochemical tests. M.P. measured the ICP-MS data. F.S., M.M.B., B.L-K, CSH, HMC, C.C. and X.L.H analyzed the data. X.L.H wrote the paper, with inputs from all other co-authors. H.M.C, C.C and X.L.H directed the research.

Materials and Methods

Reagents and materials

All reagents were analytical grade and used as received without further purification. Ni foam (with thickness 1.6 mm and 95% porosity) was purchased from Goodfellow Cambridge Ltd., UK, hydrochloric acid (HCl) and potassium hydroxide (KOH) were purchased from Merck KGaA, Germany. The water used throughout all experiments was deionized water.

Preparation of the electrodes

NF: The as-received nickel foam was washed with acetone under sonication condition for 15 min.
NF-AC: The NF sample was cleaned in 10 wt% HCl under sonication condition for 30 min.
NF-AC-FD: The NF-AC sample was dipped in 50 mL of freshly prepared $FeCl_3$ solution (0.01 M) under magnetic stirring for 15 min. The NF-AC sample was taken out and directly dried in oven at 70 ^{0}C.
Au-NiO_x: NiO_x was electrodeposited on Au (100 nm) coated Fluorine-doped tin oxide (FTO) substrates (there is a sputtered 10 nm Cr adhesion layer between the Au and FTO layers). The surface area is 1 cm^2. Prior to each deposition, the Au-coated FTO was electrochemically cycled three times from -0.2 to 0.6 V vs Ag/AgCl reference electrode at 10 mV s^{-1} in 1M Fe free KOH. NiO_x was electrochemically deposited from a nitrogen-purged nickel nitrate solution (0.01M) at a cathodic current density of 1 mA cm^{-2}, following a modified literature procedure[1]. The typical deposition time was 75 s. To change the quantity of NiO_x, the deposition time varied from 75 s to 300 s.
GC-NiO_x: NiO_x was electrodeposited on glassy carbon (GC, the geometric surface area is confined to 0.5 cm^2). The deposition procedure is the same as for Au-coated FTO.

Preparation of reference samples for Raman test

γ-FeOOH: 20 mL of $Fe(NO_3)_3$ solution (20 mM) was sealed in a glass container, which was then maintained at 60 ^{o}C for 24 h. After centrifuging and washing with water for 3 times, red brown powder of FeOOH was obtained.
γ-NiOOH was synthesized by oxidizing nickel foam with $K_2S_2O_8$ in concentrated NaOH (see reference [2]). γ-Fe_2O_3 was obtained by annealing Fe_3O_4 nanoparticles (Sigma-Aldrich, CAS number: 1317-61-9) at 300 ^{o}C in air for 12 h. α-Fe_2O_3 was purchased from Fluka (CAS number: 1309-37-1). NiFe LDH was synthesized via a hydrothermal method previously reported by our group (see reference [3]).

Preparation of $NiFeO_x$ catalysts.

To compare with the state-of-the-art $NiFeO_x$ catalyst, we prepared samples of $NiFeO_x$ on GC and NF electrodes following the reported electrodeposition method [4,5]. To avoid the formation of our catalyst during the electrodeposition, the NF was firstly annealed at 500 ^{o}C in air for 2 h. Films of $NiFeO_x$ were cathodically deposited from unstirred solutions of 0.092 M $Ni(NO_3)_2{\cdot}6H_2O$ and 0.008M $FeCl_2{\cdot}4H_2O$ (or 0.0975M $Ni(NO_3)_2{\cdot}6H_2O$ and 0.0025M $FeCl_2{\cdot}4H_2O$) in 18.2 MΩ·cm H_2O. The solutions were purged with nitrogen gas for half an hour before adding $FeCl_2{\cdot}4H_2O$ to prevent precipitation of insoluble FeOOH. Typical depositions were at -0.1 mA cm^{-2} for 20-180 s.

Characterization

SEM images were taken with a Phillips (FEI) XLF-30 FEG scanning electron microscope. EDS-SEM spectra were taken from the spectrometer attached to a Phillips (FEI) XLF-30 FEG scanning electron microscope. XPS measurements were performed on a PHI5000 VersaProbe II XPS system by Physical Electronics (PHI) with a detection limit of 1 atomic percent. Monochromatic X-rays were generated by an Al Kα source (1,4867 eV). The diameter of the analyzed area is 10 μm.

Raman spectra were recorded using a confocal Raman microscope (Renishaw). Spectra were acquired with <0.32 mW of 532 nm laser excitation at the sample surface. The exposure time is 3 s and the 50 spectra were accumulated. For each material, three samples were tested, and for each sample several points were randomly chosen to take Raman spectrum on. For samples after OER, Raman spectra were recorded after chronoamperometry scan at η = 310 mV for around 10 min. For reference samples, their Raman spectra were similar to those reported in literature works [1,6,7]).

ICP-MS measurements were conducted on a Finnigan™ element2 high performance high resolution ICP-MS, which consists of a double focusing reverse geometry mass spectrometer. The sensitivity was better than $1.2x10^5$ cps/ppb of ^{115}In at a mass resolution of 4000, which corresponds to $1.2x10^6$ cps/ppb at low resolution mode of 500. Measurement repeatability expressed in terms of RSD was better than 5%, depending on the element. The accuracy of the method was tested using certified riverine water reference materials SLRS-3. Accuracy was better than 5%. The detection limits obtained for trace metals in the Medium resolution mode (R=4000) without the influence of signal interferences were in routine mode less than 0.2 ng L^{-1} for all elements. Calibration standards were prepared through successive dilutions in cleaned Teflon bottles, of 1g L^{-1} ICP-MS stock solutions (Bernd Kraft). Suprapur® grade nitric acid (65% Merck) was used for the dilution of samples and for the preparation of standards (2+1000). Ultrapure water was produced using Milli-Q® Ultrapure Water System (Millipore, Bedford, USA). The high resolution mode is also useful for samples having unexpected or unknown interferences, because the quantification is obtained by integrating only the area of the analyte peak, without the influence of an unexpected interference peak.

ICP-MS sample preparation: For the testing of Fe concentration in KOH, 1 M KOH solution (Merck KGaA) was neutralized by adding ultrapure nitric acid (65%, Merck KGaA). To test the concentration of Fe on the catalysts surface, NF-AC-NiO_x-Fe (electrode area: 1.0-1.1 cm^2) was dipped in ultrapure nitric acid (mixture of 0.25 mL ultrapure nitric acid (65%, Merck KGaA) and 5 mL H_2O) for 1-2 min, washed with distilled water twice. Dipping in nitric acid for a longer time led to same results. All the nitric acid and washing water were collected. Water was then added to reach the total volume of 10 mL. To make sure all the surface Fe was dissolved in nitric acid, the treated samples were checked by testing the OER activity in Fe free 1M KOH. The OER activity is similar to NF-AC in Fe-free 1M KOH, indicating the total dissolution of surface Fe. The loading examined in this method is also close to the value calculated from the Fe concentration change before and after 100 CVs activation of NF-AC in 1M KOH (60 mL). This confirmed the total dissolution of Fe on NF-AC-NiO_x-Fe surface. To be consistent with literature data, the loadings were referred to iron oxide, assuming a Fe_2O_3 formula. A variation in the formula will only introduce negligible uncertainty in the comparison.

Electrochemical measurements

Electrochemical characterizations including cyclic voltammetry (CV), linear sweep voltammetry (LSV), and chronopotentiometry were carried out on a Gamry Reference 3000 electrochemical instrument using a three-electrode electrochemical system. A 1M KOH solution (60 mL) was used as electrolyte, and an Ag/AgCl electrode with saturated KCl filling solution and Pt wire were used as reference and counter electrodes, respectively. Nickel foams were used as working electrodes directly. Hot glue was used to define the working area as a 1.0-1.1 cm^{-2} zone. Before electrochemical measurements, the reference electrode was measured against another unused Ag/AgCl reference electrode stored in saturated KCl solution. Calibration of Ag/AgCl reference electrodes was done by measuring the RHE potential using a Pt electrode under a H_2 atmosphere. During the measurements, Ag/AgCl reference electrode was set into a double-junction electrode to minimize contact between KOH and KCl. CVs were performed at a scan rate of 1 mV s^{-1}, and the average of the two potentials at which the current crossed zero was taken to be the thermodynamic potential for the hydrogen electrode reaction. In 1M KOH electrolytes, E vs. RHE = E vs. Ag/AgCl + 1.009 V, and overpotential for OER was η = E vs. RHE -1.23 V = E vs. Ag/AgCl – 0.221 V. Ohmic drop correction was performed using the current interrupt (CI) method available in the potentiostat software.
Before recording the catalytic activity, catalysts were activated by 5 linear sweeping voltammetry (LSV) scans followed by another 100 cyclic voltammetry scans until reaching a stable state in 1M KOH (~30 mL). The LSV scans were recorded in the potential range 0.6-0.38 V vs Ag/AgCl at a scan rate of 1 mV s^{-1}. The cyclic voltammetry scans were recorded in the potential range 0.2-0.53 V vs Ag/AgCl at a scan rate of 10 mV s^{-1}. Following this, 2-3 cycles of backward LSVs were measured at a scan rate of 1 mV s^{-1} to record the catalytic activity. Tafel slopes were calculated based on the LSV curves by plotting overpotential against log(current density). Chronopotentiometric measurements were performed to evaluate the long-term stability. For the loading dependence analysis, loadings were tuned by changing the cycling number of CVs or only applying 1-5 LSVs. Besides NF-AC, Au-NiO_x and GC-NiO_x were activated using the same procedure.

Calculation of the specific current density, J_s:

AC impedance measurements were taken over the frequency range of 100 Hz to 0.1 kHz. Impedance measurements were taken on charged catalysts at 0.501, 0.481 and 0.461 V versus Ag/AgCl (*ACS Catal.*, 2015, 5 (11), pp 6680–6689). The double-layer capacitance values (C_{dl}) were obtained through fitting of the impedance spectrum using an equivalent circuit (Voigt circuit, see below) with two characteristic time constants[8].

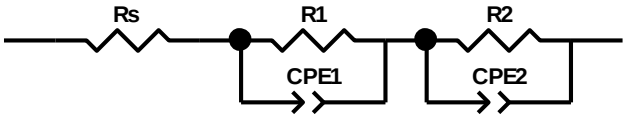

The electrochemically active surface area (ECSA) was calculated from the double-layer capacitance according to the equation below:

$$ECSA = C_{dl}/C_s$$

Where C_s is the specific capacitance. C_s is 81 uF cm^{-2} for Ni(Fe)O_x [9].

The roughness factor (RF) was calculated by taking the estimated ECSA and dividing it by the geometric area of the electrode (normally 1 cm^2). The specific current density J_s was calculated according to equation below:

$$J_s = J/RF$$

Where J is the geometric current density.

Calculation of J_s of $NiFeO_x$ from data in the literatures[9,10]:

The $NiFeO_x$ sample obtained by continuous deposition and described in a recent paper[9] was chosen as a state-of-the-art sample. At the loading of 300 nmol of metal per cm^{-2}, the TOF is ca. 0.18 s^{-1}. So the geometric current density is

J = TOF * 4 n F = 0.18 s^{-1} x 4 x (300 x 10^{-9}) mol.cm^{-2} x 96485 C mol^{-1}= 0.0208 A.cm^{-2} = 20.8 mA.cm^{-2}

At the loading of 300 nmol of metal per cm^{-2}, the capacitance C_{dl} is ca. 20 mF.cm^{-2}.

The roughness (RF) is therefore

RF = C_{dl}/C_s= 20 mF.cm^{-2}/0.081 mF.cm^{-2}= 247 (taking Cs as 0.081 mF.cm^{-2}, which is the value we used to calculate the RF for our reference $NiFeO_x$ samples)

J_s = J/RF = J/247 = 0.084 mA.cm^{-2}.

This value is similar to the one determined in the current work (0.13±0.02 mA.cm^{-2}) for the reference $NiFeO_x$ sample on GC.

For another state-of-the-art sample of $NiFeO_x$ [10], the J_s was reported at an overpotential of 350 mV: $J_{s,\eta=0.35\ V}$ = 3 ± 2 mA cm^{-2}. Considering a Tafel slope of 35 mV/dec, the J_s at 300 mV is $J_{s,\eta=0.30\ V}$ = 0.11 ± 0.07 mA cm^{-2}, which is again similar to the value determined in the current study (0.13±0.02 mA cm^{-2}).

Calculation of Turnover frequency (TOF)

The TOF value was calculated from the equations:

$$TOF = \frac{J \times A}{4 \times F \times m}$$

where J is the current density at a given overpotential (e.g. η =250, 270, and 300 mV), A is the geometric surface area of the electrode, F is the Faraday constant (a value of 96485 C mol^{-1}), and m is the number of moles of Fe on the electrode. For our samples, the Fe loadings are measured by ICP-MS.

Supplementary Fig. 2b shows the potential-dependent TOFs for five electrodes with an iron oxide loading of 1.0-14.1 μg cm^{-2}. Supplementary Table S1 gives the TOFs of 11 individual electrodes. Except at the lowest loading, i.e, 1.0 μg cm^{-2}, the TOFs of samples with different loadings in this range are similar. The TOFs at 1.0 μg cm^{-2} are significantly higher, in agreement with recent observations that at an ultralow loading (≤ 1 μg cm^{-2}) the TOFs of

certain OER catalysts were abnormally high compared to the same catalysts at loadings between 1.4 to 14.1 μg cm^{-2}. A "substrate effect"[11] or "nucleus sintering" [12] was invoked to rationalize these observations. The intrinsic activity, however, is best represented by TOFs at higher loadings [12].

XAS Data collection.

Ex-situ XANES data were collected on the LUCIA beamline of SOLEIL [13], at an energy of 2.75 GeV and with a ring current of 100 mA (8-bunch mode). The incident beam energy was monochromatized using a Si 111 double crystal monochromator. The electrochemical *in-situ* XAS were recorded at SP8 (Japan) 12B2 Taiwan beamline of National Synchrotron Radiation Research Center (NSRRC), the electron storage ring was operated at 8.0 GeV with a constant current of ~100 mA. The *in-situ* XAS measurement was performed at the desired voltage to keep the situation of reduction with a special cell designed for these experiments. The photon energy was calibrated with the first inflection point of Fe K-edge and Ni K-edge in Fe and Ni metal foils, respectively. XAS data were collected in either total electron yield mode or fluorescence mode.

XAS data analysis and EXAFS fittings.

The data collected were normalized to the incoming incident photon flux and processed with the Athena software from the IFEFFIT package. E_0 values of 7112.0 eV and 8333.0 eV were used to calibrate all data with respect to the first inflection point of the absorption K-edge of either iron or nickel foil, respectively.

EXAFS curve fitting was performed with Artemis and IFEFFIT software using *ab initio*-calculated phases and amplitudes from the program FEFF 8.2 [14,15]. These *ab initio* phases and amplitudes were used in the EXAFS equation:

$$\chi(k) = S_0^2 \sum_j \frac{N_j}{kR_j^2} f_{eff,j}(\pi, k, R_j) e^{-2\sigma_j^2 k^2} e^{-2R_j/\lambda_j(k)} \sin[2kR_j + \phi_{ij}(k)]$$

The neighboring atoms to the central atom(s) are divided into *j* shells, with all atoms with the same atomic number and distance from the central atom grouped into a single shell. Within each shell, the coordination number N_j denotes the number of neighboring atoms in shell *j* at a distance of R_j from the central atom. $f_{eff,j}(\pi, k, R_j)$ is the *ab initio* amplitude function for shell *j*, and the Debye-Waller term $e^{-2\sigma_j^2 k^2}$ accounts for damping due to static and thermal disorder in absorber-backscatterer distances. The mean free path term $e^{-2R_j/\lambda_j(k)}$ reflects losses due to inelastic scattering, where $\lambda_j(k)$ is the electron mean free path. The oscillations in the EXAFS spectrum are reflected in the sinusoidal term $\sin(2kR_j + \varphi_{ij}(k))$, where $\varphi_{ij}(k)$ is the *ab initio* phase function for shell *j*. S_0^2 is an amplitude reduction factor due to shake-up/shake-off processes at the central atom(s). The EXAFS equation was used to fit the experimental data using CN, R, and the EXAFS Debye-Waller factor (DW; σ^2) as variable parameters. For the energy (eV) to wave vector (*k*, $Å^{-1}$) axis conversion, the S_0^2 value was determined as 0.90. All fits were performed in the R space. The R-value (%) is employed to judge whether a fitting is proper, and is expressed by the following equation:

$$\boldsymbol{R} = \Sigma\{k^n \chi_{obs}(k) - k^n \chi_{cal}(k)\}^2 / \Sigma\{k^n \chi_{0bs}(k)\}^2$$

Computational Details

All computations were performed using the GPAW code [16,17] in combination with the Atomic Simulation Environment (ASE) (https://wiki.fysik.dtu.dk/ase/). The RPBE[18] exchange correlation functional together with a 0.17 Å grid spacing and a 1x5x1 k-point set for γ-FeOOH or a 5x5x1 k-point set for γ-NiOOH was used. H_2O and H_2 were modeled using only the Γ-point. The core electrons were approximated through Projector Augmented Wavefunctions (PAW)[19]. A smearing of 0.1 eV was added to facilitate the convergence of the wavefunction. Following previous work[20], the spin was treated explicitly assuming a high-spin configuration on Fe and a low spin configuration on Ni. Ferromagnetic coupling between the ions was used. Assuming a ferromagnetic coupling reduces the complexity of the computation significantly while only introducing a minor additional error bar. Assuming a Neel temperature of 1000 K the uncertainty between the assumed and real magnetic coupling would correspond to an additional error of approximately 0.1 eV. This procedure has been applied successfully to a large number of materials.[20,21]. The geometries were optimized using the BFGS algorithm and convergence was assumed if the forces were below 0.05 eV/Å. The final redox potentials and adsorption potentials were computed using the theoretical Normal Hydrogen Electrode described by Rossmeisl *et al.* [22,23] assuming a constant set of corrections for Zero-point energies and entropy effects.

γ-NiOOH and γ-FeOOH were modeled in independent unit cells. Both compounds display a brucite type crystal structure. γ-FeOOH model is obtained by cutting the lattice along the (010) plane. A 4-monolayer slab with 2 monolayers being fixed to bulk positions in combination with a 2x1 surface is used. A vacuum of 14 Å along the x-axis and 9 Å along the z axis is added to avoid interactions between the slabs. γ-$Ni(OH)_2$ and γ-NiOOH were modeled using a single layer assuming oxidation and reduction of threefold M-OH and M=O species. γ-NiOOH edge and corner sites as well as NiO were excluded based on their high redox potentials reported in literature [24,25]. Following the state–of-the-art procedure in computational electrochemistry [26] solvent and double layer effects were neglected. This procedure is known to semi-quantitatively reproduce experimental trends [24,25,27,28].

In agreement with current high level publications in the field [24,25,27,28], we limited our computations to a "thermodynamic only" picture. This is due to the fact that activation barriers in electrocatalysis can be expected to be strongly influenced by the detailed structure of the double layer. This is especially true for reaction steps comprising the abstraction or transfer of H^+/e^- couples. Additionally, both the mono-nuclear and bi-functional formation of the O-O bond bears significant mechanistic similarities. In both cases a nucleophile (OH^- or H_2O) attacks a Fe=O unit. Indeed, the superiority of the bi-functional mechanism lies not in differences in the details of the O-O bond formation step but in the ability to form a thermodynamically more favorable final state via H-transfer to an acceptor species. Thus, assuming a negligible O-O bond formation barriers for both mechanisms, the "thermodynamic only" is able to capture the differences between both reaction paths. Moreover, it has been shown that the potential limiting kinetic barriers for OER on a number of active metal oxides such as G-FeCoW and $NiFeO_x$ are small compared to thermodynamics (less than 1 eV) [26].

Construction of Volcano Plot

In the volcano plot, the redox potential of the oxidation form M-OH to M=O is used as a descriptor. To construct a volcano plot, linear scaling relations between the water oxidation intermediates M-OH, M=O and M-OOH are required. Following previous work [25,29], we assume:

$$\Delta G(M=O) = 2\Delta G(M-OH) \quad \text{(Equation S1)}$$

$$\Delta G(M-OOH) = \Delta G(M-OH) + 3.2eV \quad \text{(Equation S2)}$$

Water and hydrogen are taken as reference states, i.e.

$$G(H_2O) = G(H_2) = 0eV \quad \text{(Equation S3)}$$

and the experimental values of 4.92 eV is used for oxygen.

$$G(O_2) = 4.92eV \quad \text{(Equation S4)}$$

a) Mono-nuclear mechanism:

At the strong binding side (left slope in Figure S5a), the formation of the O-O bond is potential determining:

$$M=O + H_2O \rightarrow M-OOH + H^+ + e^- \quad \text{(Equation S5)}$$

Subtracting the overpotential of 1.23 eV from the reaction energy one obtains:

$$-\eta_1 = -\{[\Delta G(M-OOH) - \Delta G(M=O)] - 1.23eV\} \quad \text{(Equation S6)}$$

Inserting equation S2, the theoretical overpotential becomes

$$-\eta_1 = [\Delta G(M=O) - \Delta G(M-OH)] - 1.97eV \quad \text{(Equation S7)}$$

At the weak binding side (right slope in Figure S5a), the overpotential is determined by the oxidation of M-OH to M=O.

$$M-OH \rightarrow M=O + H^+ + e^- \quad \text{(Equation S8)}$$

Accordingly, the overpotential is given by

$$-\eta_2 = -[\Delta G(M=O) - \Delta G(M-OH)] + 1.23eV \quad \text{(Equation S9)}$$

b) Bi-functional Mechanism

The bi-functional mechanism only influences the energetics of the O-O bond formation step. Accordingly, the weak binding side is given by equation S9. At the top of the volcano the recovery of the hydrogen acceptor unit Ni_3-O determines the overpotential.

$$Ni_3-OH \rightarrow Ni_3-O + H^+ + e^- \quad \text{(Equation S10)}$$

Since this step is independent of the descriptor the top becomes a flat line. With

$$\Delta G(Ni_3-OH \rightarrow Ni_3-O) = 1.3eV \quad \text{(Equation S11)}$$

the overpotential becomes:

$$-\eta_3 = -0.07eV \quad \text{(Equation S12)}$$

The strong binding side is replaced by the bi-functional formation of the O-O bond:

$$M = O + Ni_3 - O + H_2O \rightarrow M + O_2 + Ni_3 - OH + H^+ + e^- \quad \text{(Equation S13)}$$

the corresponding theoretical overpotential can then be obtained through

$$-\eta_4 = -\{[G(O_2) + G(Ni_3 - OH)] - \Delta G(M = O) + G(Ni_3 - O)] - 1.23\}$$
(EquationS14)

According to equation S1, the energetics of the reaction step M-OH to M=O is equivalent to ΔG(M-OH). Inserting also ΔG(O_2) from equation S4 and ΔG(Ni_3-OH→Ni_3-O) from equation S11 gives:

$$-\eta_4 = 2[\Delta G(M = O) - \Delta G(M - OH)] - 2.39 \quad \text{(Equation S15)}$$

Zero-point Energy and Entropy Corrections

Reaction	ZPE + TΔS [eV]
$M + H_2O \rightarrow M\text{-}OH + 0.5\ H_2$	0.4
$M + H_2O \rightarrow M{=}O + H_2$	0.05
$M + 2\ H_2O \rightarrow M\text{-}OOH + 1.5\ H_2$	0.41

ZPE and TΔS corrections according to reference [25].

Summary of Binding Energies

System	ΔG(M-OH) [eV]	ΔG(M=O) [eV]	ΔG(M-OOH) [eV]
γ-FeOOH (010)	1.10	2.34	4.02

Redox Potentials of Hydrogen Acceptors

Hydrogen Acceptor	ΔG [eV]
Ni^{2+}_3-OH → Ni^{3+}_3=O (*)	1.2
Ni^{2+}_3-OH → Ni^{3+}_3=O (**)	1.3

(*) in Ni^{2+} embedding (**) in Ni^{3+} embedding

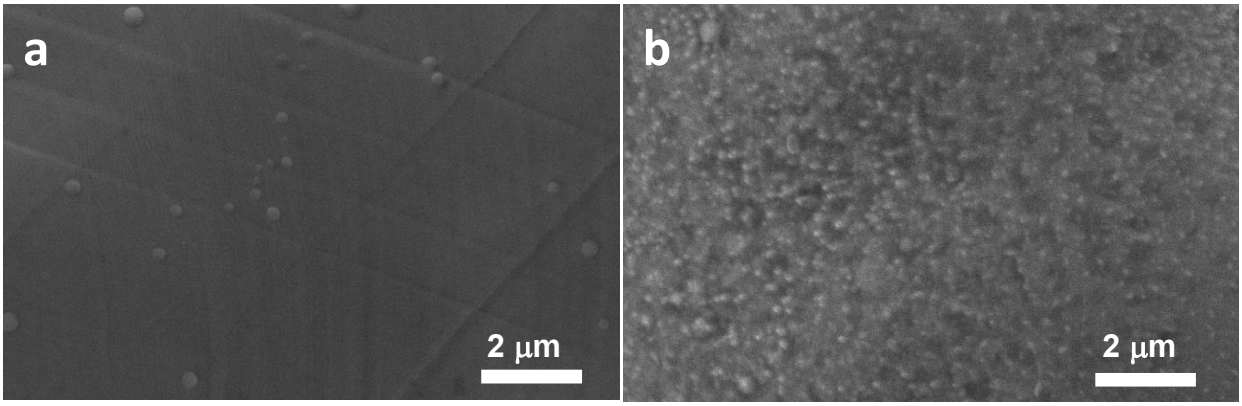

Supplementary Figure 1 | SEM images of the surfaces of (a) NF and (b) NF-AC.

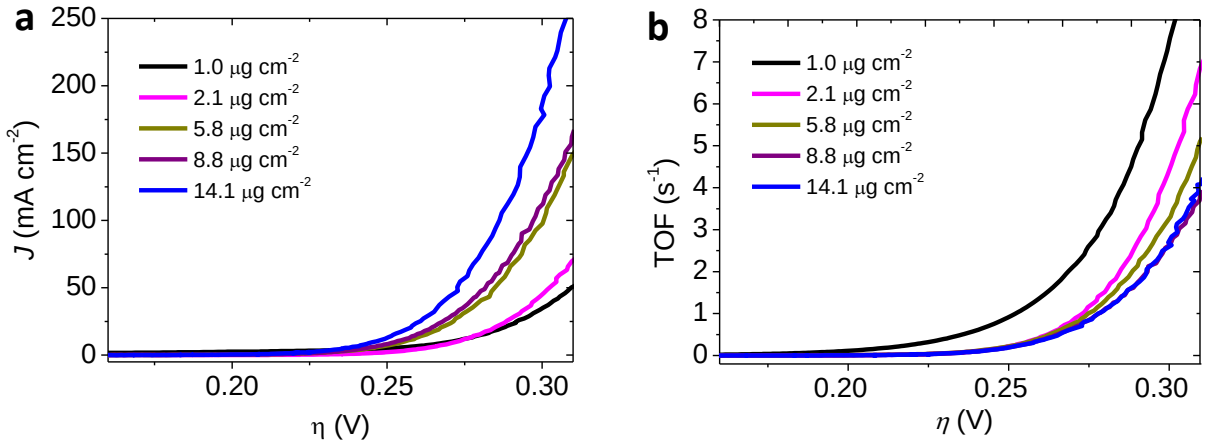

Supplementary Figure 2 | a, Polarization curves and **b**, corresponding TOFs of five representative NF-AC-NiO_x-Fe electrodes; TOFs were calculated according to the total amount of Fe ions measured by ICP-MS. Backward scan; Scan rate: 1 mV s^{-1}; IR corrected. Except at the lowest loading, i.e, 1.0 μg cm^{-2}, the TOFs of samples with different loadings in this range are similar. The TOFs at 1.0 μg cm^{-2} are significantly higher, in agreement with recent observations that at an ultralow loading (≤ 1 μg cm^{-2}) the TOFs of certain OER catalysts were abnormally high compared to the same catalysts at loadings between 1.4 to 14.1 μg cm^{-2}. A "substrate effect"[11] or "nucleus sintering" [12] was invoked to rationalize these observations. The intrinsic activity, however, is best represented by TOFs at higher loadings [12].

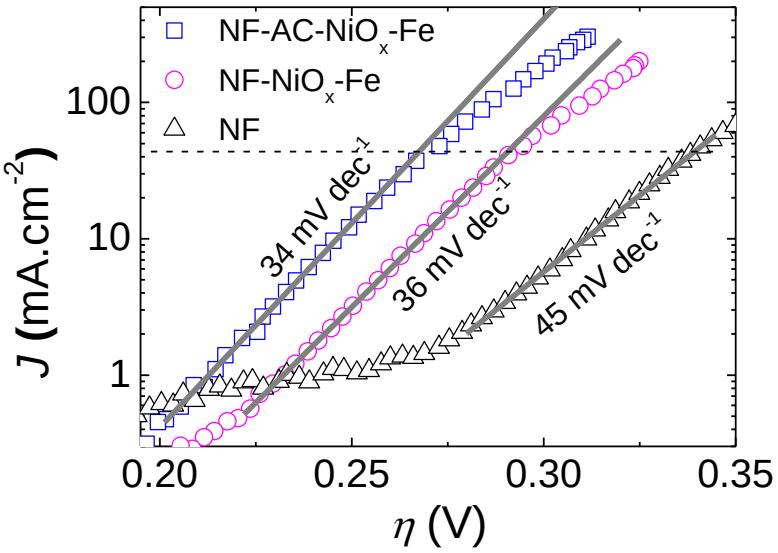

Supplementary Figure 3 | Tafel plots of NF, NF-NiOx-Fe and NF-AC-NiOx-Fe. The Tafel plots for NF-NiOx-Fe and NF-AC-NiOx-Fe are based on the 1st LSV after 100 CVs' activation. The Tafel plot of NF is based on the 1st LSV before 100 CV's activation. The loading of Fe in NF-AC-NiOx-Fe is 14.1 μg cm^{-2}, and in NF-NiOx-Fe is 4.3 μg cm^{-2}. The deviation of experimental data from the Tafel line above η = 300 mV indicates the influence of mass transport.

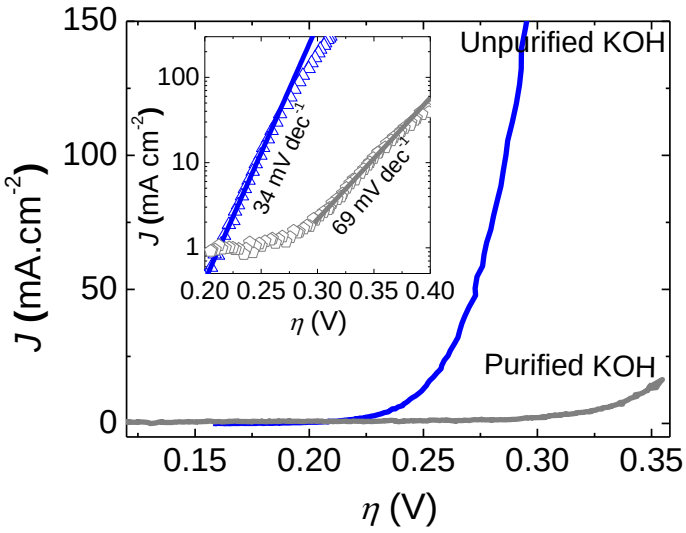

Supplementary Figure 4 | Polarization curves of NF-AC activated in unpurified KOH and purified KOH (Fe-free). Backward scan; Scan rate: 1 mV s^{-1}; IR corrected. The inset shows the corresponding Tafel plots.

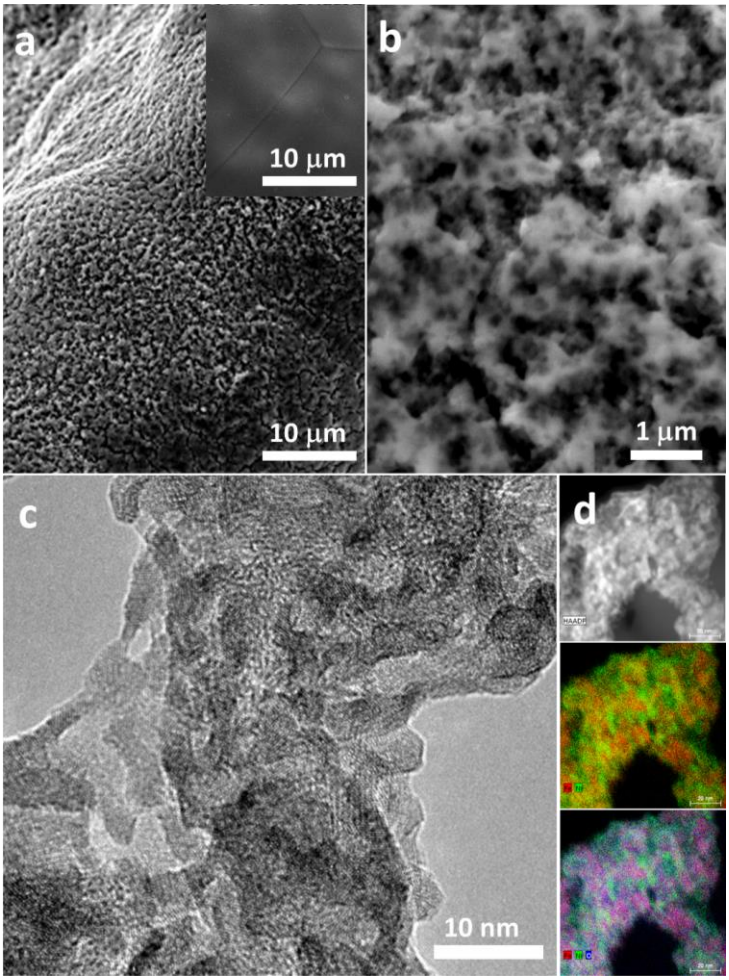

Supplementary Figure 5 | Characterization of NF-AC-FD. **a, b**, SEM images; **c,** TEM images. The inset in **a**) shows the SEM image of NF-AC. **d**, HAADF and corresponding elemental mapping images of the surface layer. Color codes: red for Fe; green for Ni; blue for O; purple for the mixture effect of Fe and O.

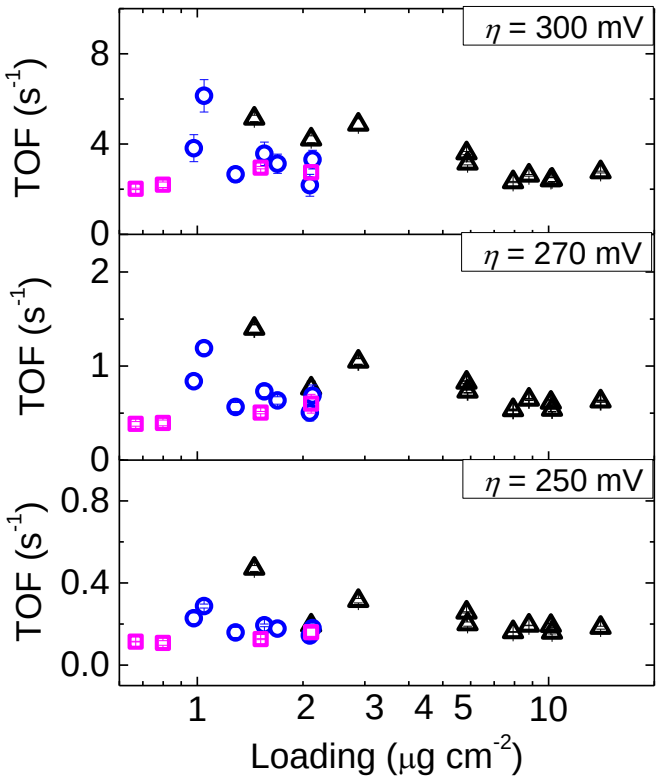

Supplementary Figure 6 | The TOFs at different loadings of iron (expressed as Fe_2O_3) for NF-AC-NiO_x-Fe (black triangles), Au-NiO_x-Fe (blue spheres) and GC-NiO_x-Fe (magenta rectangles).

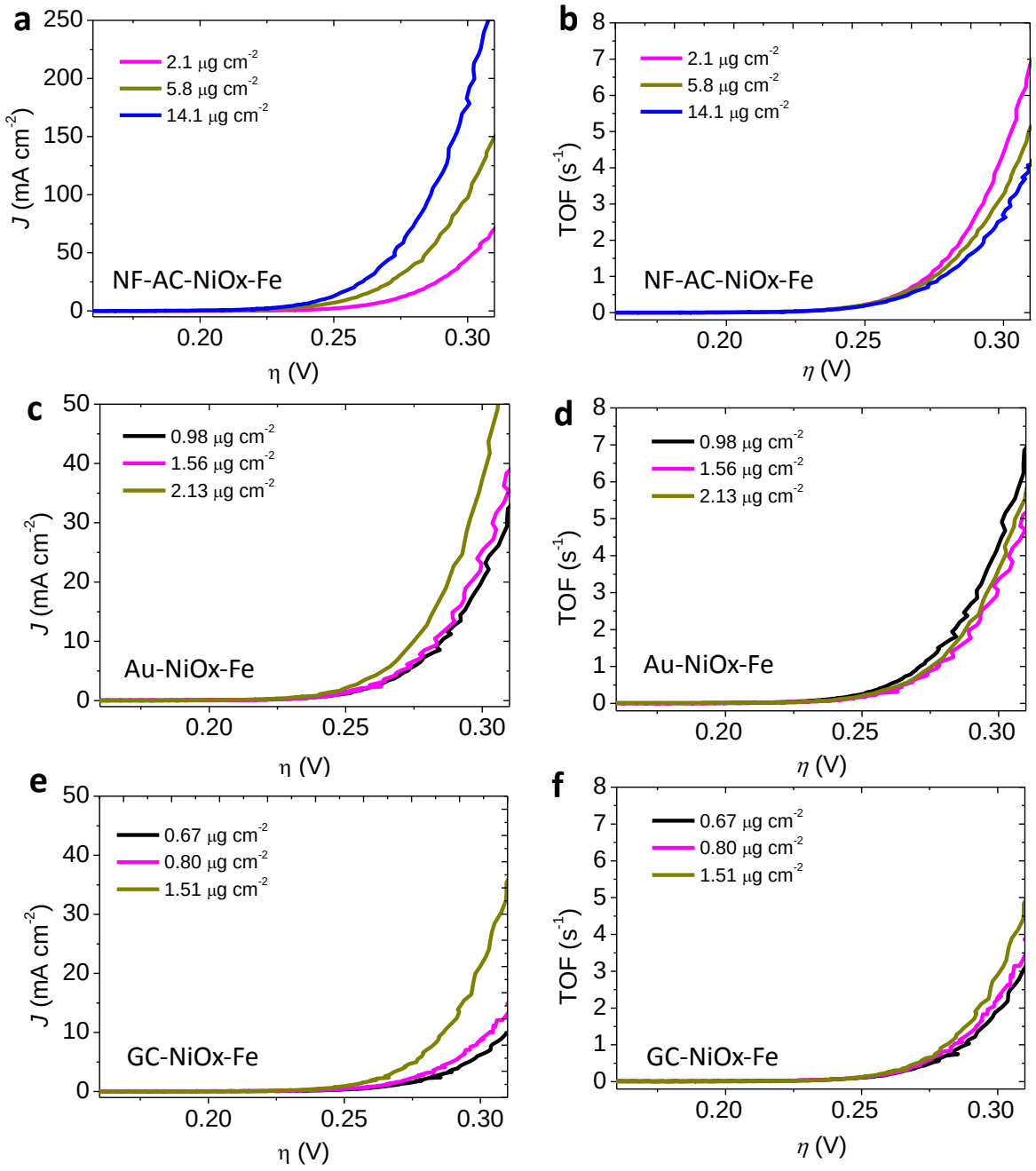

Supplementary Figure 7 | Polarization curves and corresponding TOFs of three representative samples. **a** and **b**, NF-AC-NiO_x-Fe; **c** and **d**, Au-NiO_x-Fe; **e** and **f**, GC-NiO_x-Fe. TOFs were calculated according to the total amount of Fe ions measured by ICP-MS. Backward scan; Scan rate: 1 mV s^{-1}; IR corrected.

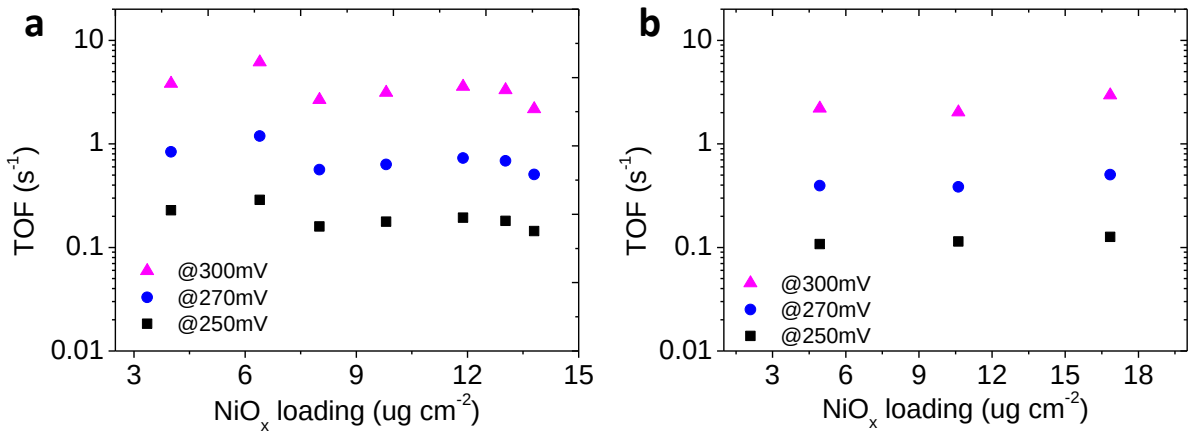

Supplementary Figure 8 | TOFs at different loadings of NiO_x. **a**, Au-NiO_x-Fe; **b**, GC-NiO_x-Fe.

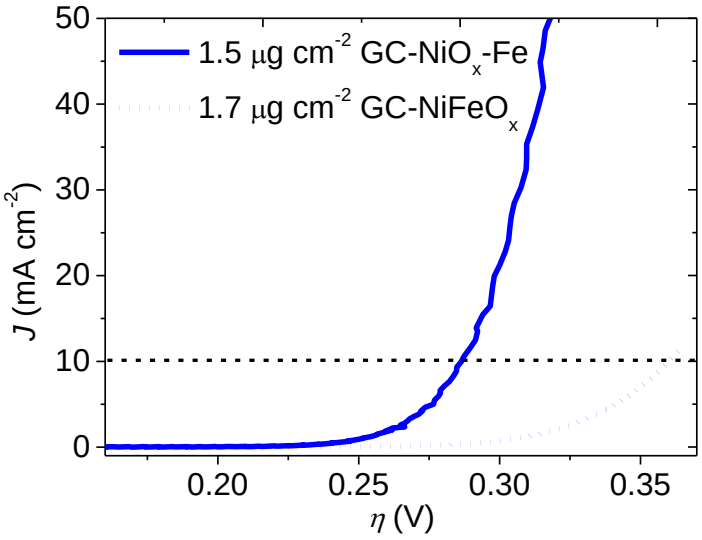

Supplementary Figure 9 | Comparison of polarization curves between GC-NiO_x-Fe and GC-$NiFeO_x$ at a similar loading.

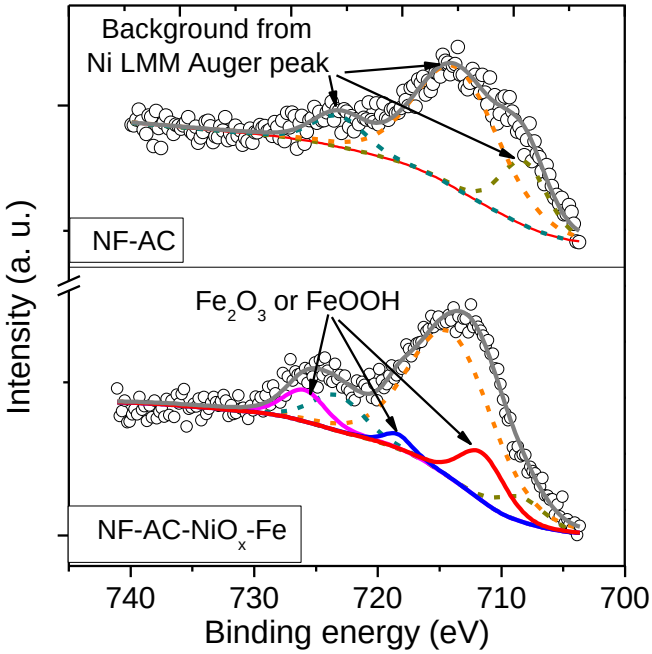

Supplementary Figure 10 | High resolution Fe 2p XPS spectra of NF-AC and NF-AC-NiO_x-Fe. The Fe 2p spectral background has contribution from Ni LMM Auger peaks [30,31]. After deduction of the background from Ni LMM Auger peaks, three residual peaks (711.5, 719.0 and 725.9 eV) in NF-AC-NiO_x-Fe can be ascribed to iron oxides deposited on the nickel foam. Due to similarities in the binding energies and spectral shapes of the higher oxides of iron, it is not possible to assign the iron species to Fe_2O_3 or FeOOH using XPS [32,33].

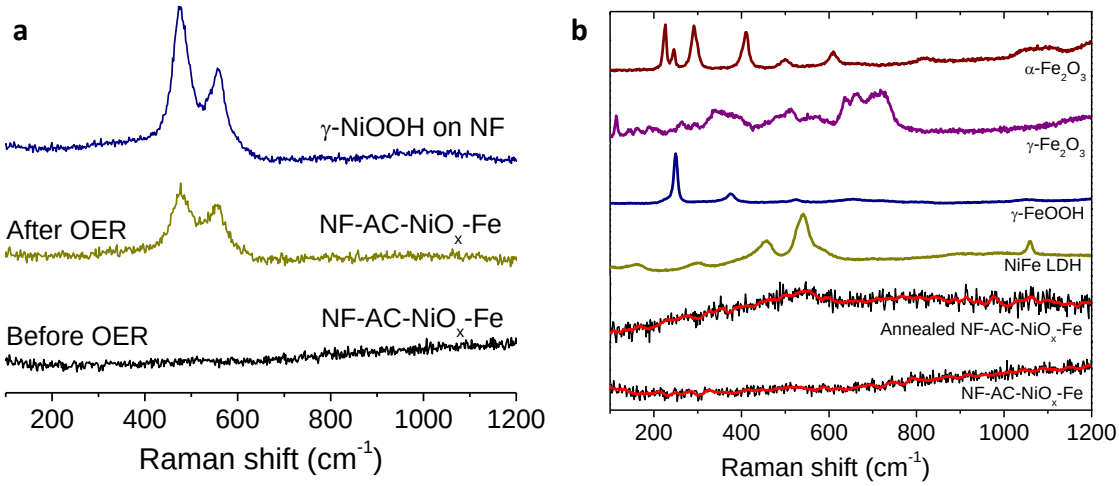

Supplementary Figure 11 | Raman spectra. a, NF-AC-NiO_x-Fe (before OER and after OER) and γ-NiOOH on NF. **b**, NF-AC-NiO_x-Fe, annealed NF-AC-NiO_x-Fe, and reference samples of NiFe LDH, γ-FeOOH, γ-Fe_2O_3, and α-Fe_2O_3. Because γ-NiOOH has a lifetime of 1 h at an open circuit, the Raman data, collected immediately before and after the catalytic test, reveal that the NiO_x component of the catalyst exists as γ-NiOOH at OER potentials. As for the iron oxide species, no characteristic peaks of crystalline hematite (α-Fe_2O_3), maghemite (γ-Fe_2O_3), lepidocrocite (γ-FeOOH), or NiFe layered double hydroxide (LDH; structurally related to Fe-doped γ-NiOOH) were observed in the Raman spectrum of the as-prepared catalyst, before or after OER. This is likely due to the low concentration of the iron oxide species.

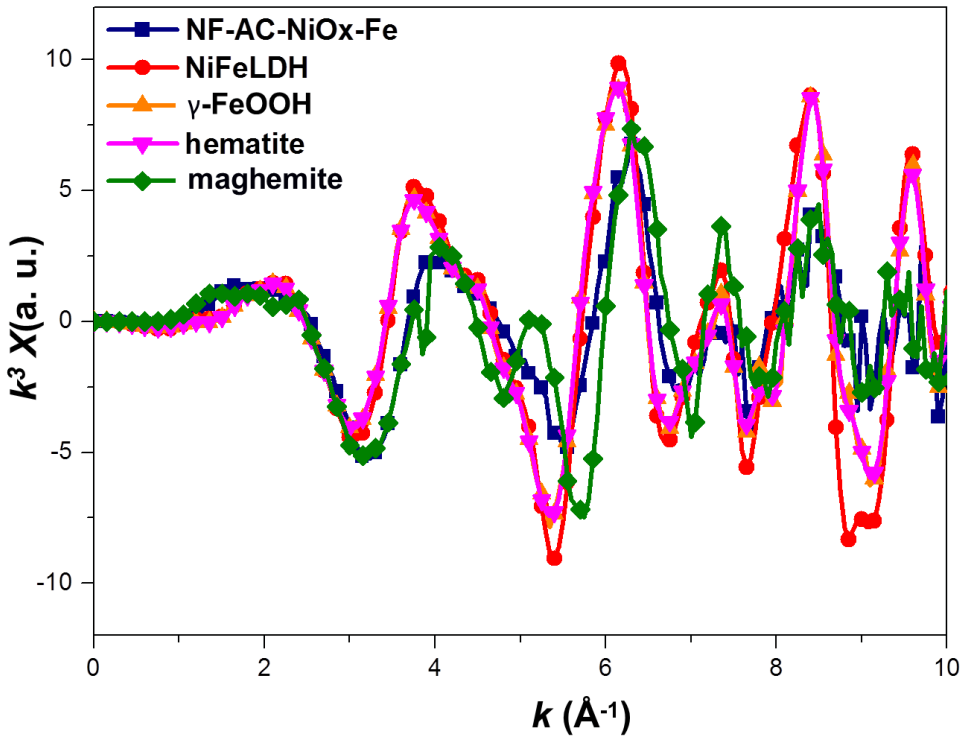

Supplementary Figure 12 | EXAFS Fe K-edge k-space spectra of NF-AC-NiO$_x$-Fe and relevant references.

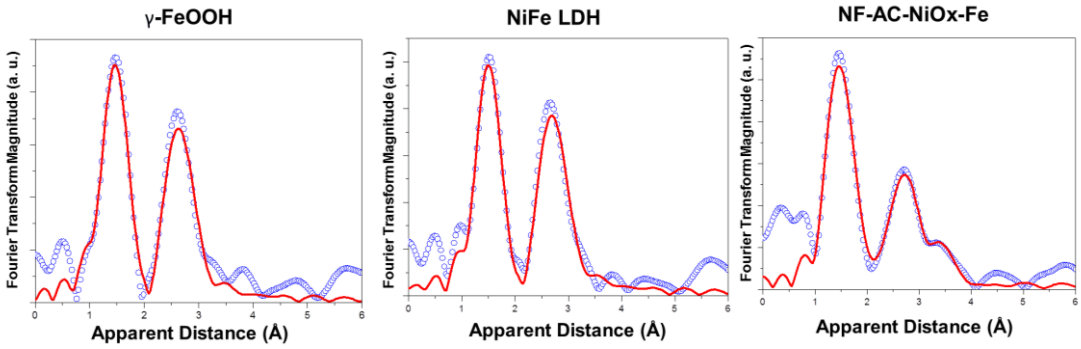

Supplementary Figure 13 | EXAFS Fe K-edge r-space spectra of γ–FeOOH, NiFe LDH and NF-AC-NiO$_x$-Fe samples extracted from EXAFS refinement, experimental data (blue circle) and the corresponding fit (red). Fitting parameters are gathered in Supplementary Table 9.

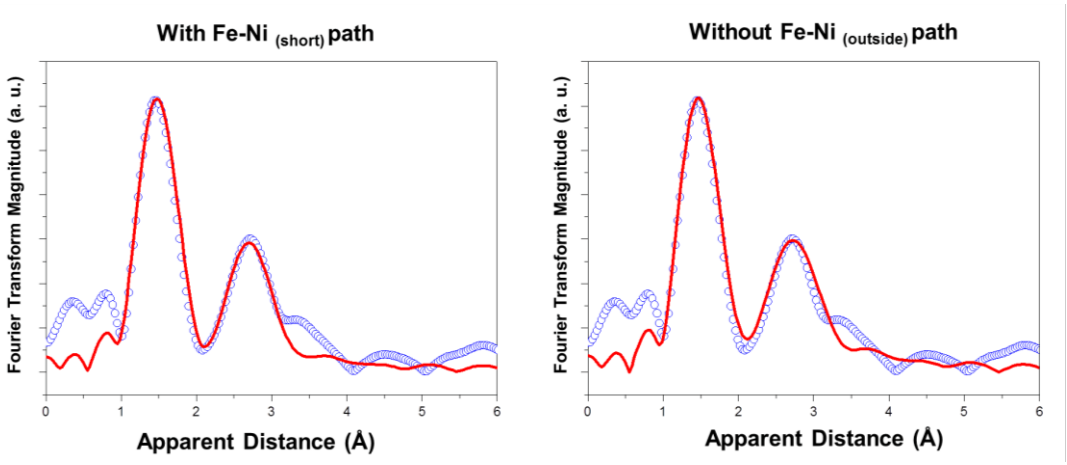

Supplementary Figure 14 | EXAFS Fourier transform Fe K-edge spectra of NF-AC-NiO_x-Fe (blue circle) and the corresponding fit (red) with Fe-Ni (short) path and without Fe-Ni (outside) path. These fittings indicate that a good fitting cannot be realized without $Fe\text{-}Ni_{(outside)}$ path. The NF-AC-NiO_x-Fe sample is lacking an $Fe\text{-}Ni_{(short)}$ path (i.e., normal NiFe LDH path) and thereby ruling out the possibility of common NiFe LDH structure.

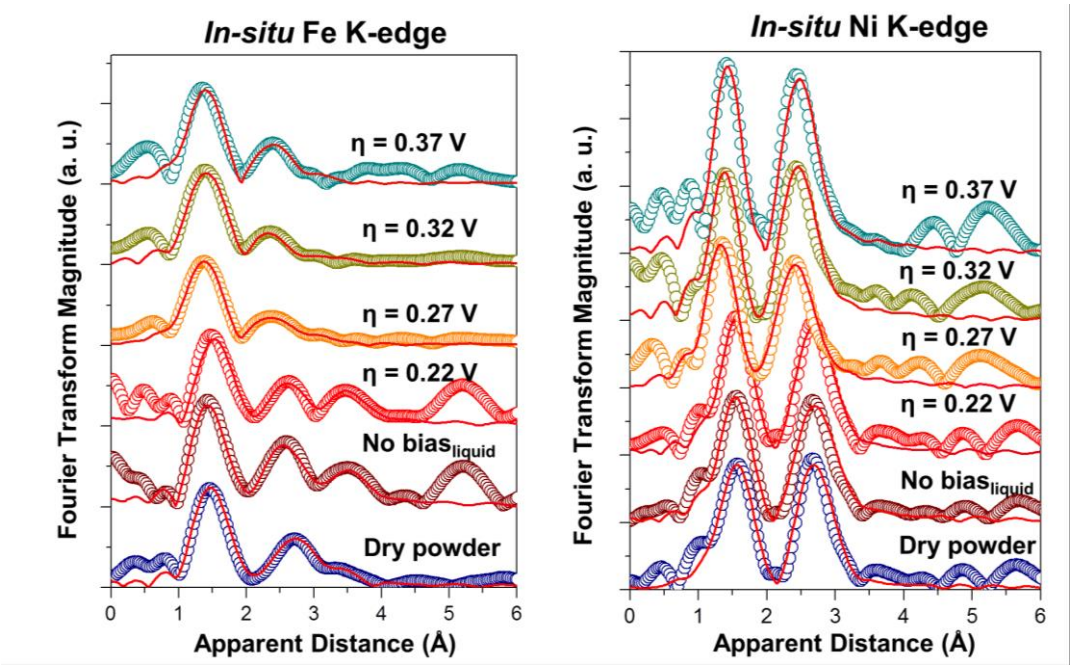

Supplementary Figure 15 | Fe and Ni K-edge EXAFS spectra (R-space) measured under *operando* conditions for the Au-NiO$_x$-Fe sample (experimental data; color circle) and the corresponding fittings (red). Fitting structural parameters are gathered in Table 2 and Supplementary Table 9.

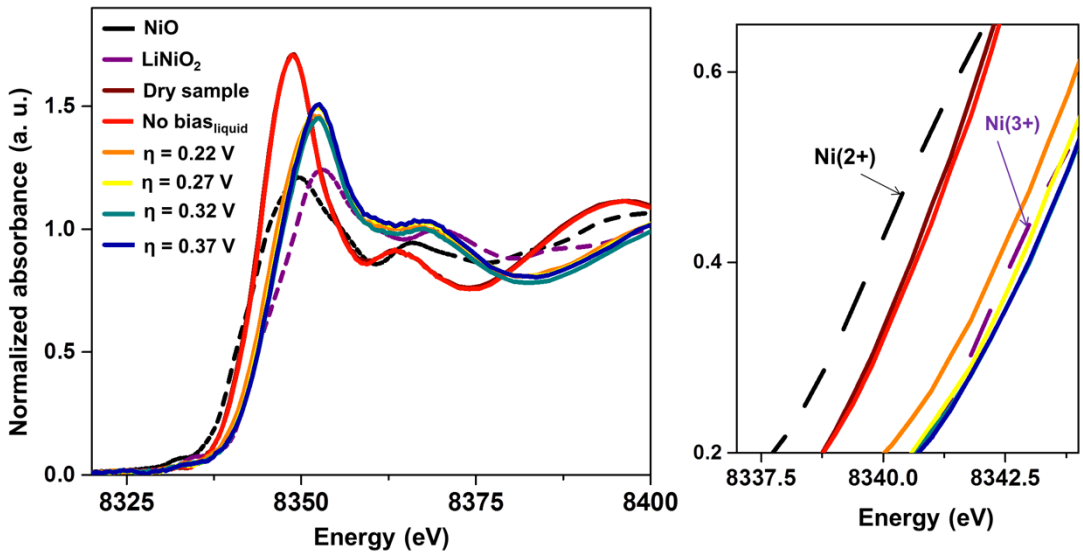

Supplementary Figure 16 | *Operando* XANES spectra of Ni K-edge for Au-NiO_x-Fe sample and the corresponding references, showing that the oxidation states of as-prepared sample in dry condition and in electrolyte (without bias) are close to +2. Once the potential is further increased to launch the OER, the oxidation states approach +3 and even higher. Ni(2+) refers to NiO, and Ni(3+) refers to $LiNiO_2$.

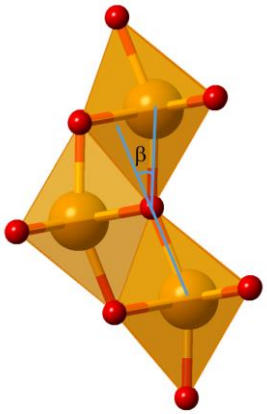

Supplementary Figure 17 | Fe-O-Fe path with 23 degree (β) tilt in γ-FeOOH

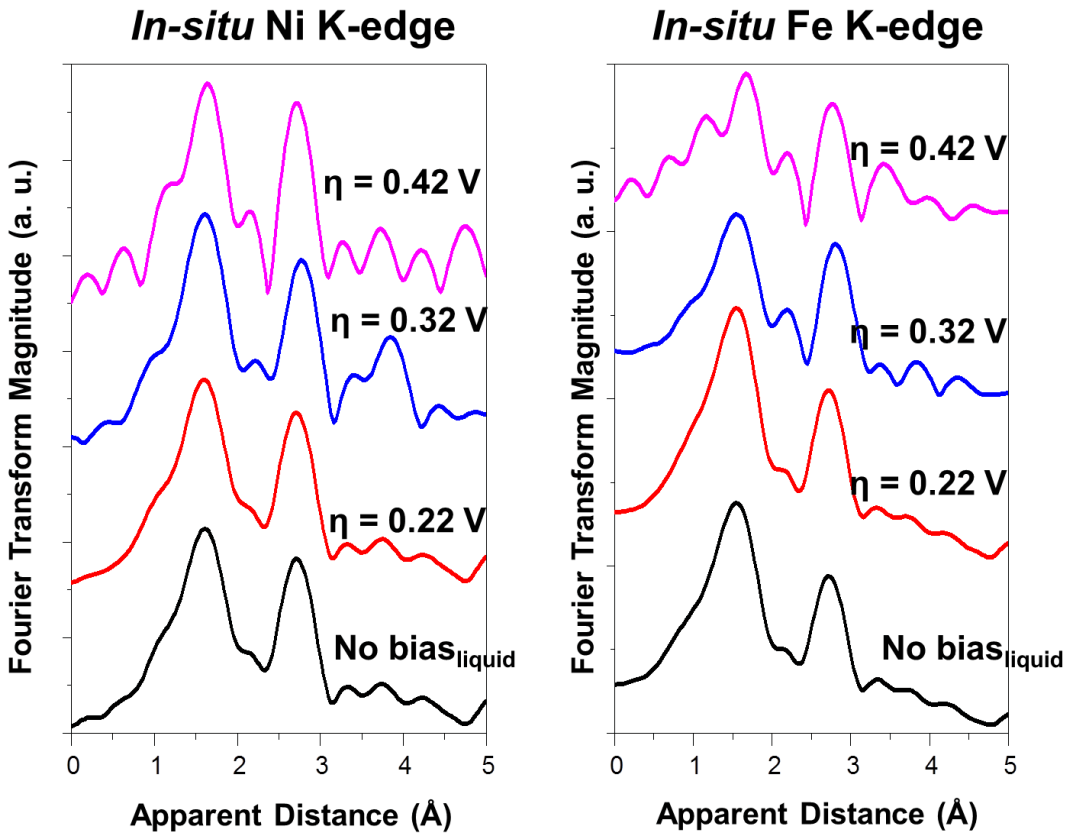

Supplementary Figure 18 | Fe and Ni K-edge EXAFS spectra (R-space) measured under *operando* conditions for the NiFe LDH sample. A large background (η = 0.42 V) present below 1 Å is due to the interference caused by generating gas bubbles.

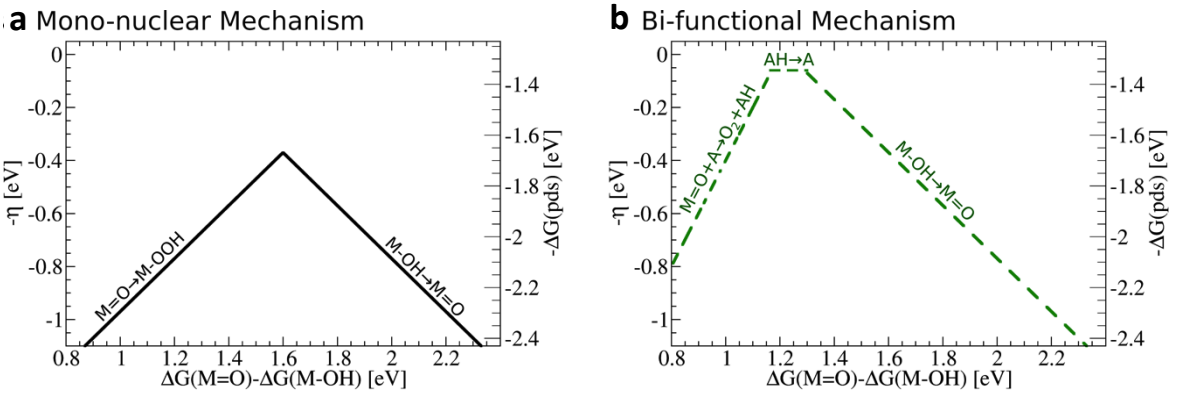

Supplementary Figure 19 | Volcano Plots. a, Mono-nuclear mechanism. **b,** Bi-functional mechanism.

Supplementary Table 1. Current densities and TOFs of all NF-AC-NiO_x-Fe electrodes (loading range: 0.96-14.07 μg cm^{-2}) at overpotentials of 250, 270, and 300 mV, respectively.

NF-AC-NiO_x-Fe	Loading (μg cm^{-2})	η@10 mA cm^{-2} (mV)	*J* (mA cm^{-2}) [a]									TOF (s^{-1}) [b]		
			250 mV			270 mV			300 mV			250 mV	270 mV	300 mV
			i	ii	iii	i	ii	iii	i	ii	iii			
1#	0.96	270	3.1	4.2	/	7.3	9.8	/	43	35	/	0.78±0.12	1.84±0.27	8.40±0.86
2#	1.46	270	3.4	3.2	/	10.1	9.5	/	37	35	/	0.47±0.02	1.40±0.04	5.14±0.14
3#	2.11	264	1.7	2.2	/	7.0	8.5	/	41.3	44.4	/	0.19±0.04	0.76±0.07	4.21±0.15
4#	2.87	264	4.5	4.2	/	15.0	14.1	/	71.0	64.0	/	0.31±0.02	1.05±0.03	4.87±0.25
5#	5.84	255	7.1	7.2	7.4	24.1	22.8	23	104	103	97.7	0.26±0.01	0.83±0.01	3.60±0.07
6#	5.89	257	5.6	5.2	6.2	20.5	20.1	21.6	88.3	86.5	93	0.20±0.02	0.73±0.02	3.15±0.07
7#	7.93	256	6.3	6.1	6.1	20.2	20.0	20.9	88.0	87.0	90.9	0.16±0.01	0.53±0.01	2.32±0.03
8#	8.80	251	8.1	8.2	8.3	26.7	27.8	27.6	108	113	112	0.19±0.01	0.64±0.01	2.62±0.04
9#	10.16	254	9.8	8.4	10	31.6	27.4	31.0	124	107	122	0.19±0.02	0.61±0.03	2.40±0.11
10#	10.22	250	8.5	7.4	7.6	28.3	24.4	26.9	127	112	121	0.16±0.01	0.54±0.02	2.43±0.09
11#	14.07	245	12.0	11.8	13.3	41.4	42.6	43.5	183	187	192	0.18±0.01	0.63±0.01	2.76±0.04

[a] Each sample is measured 2-3 times and the current densities for each measurement are listed (i, ii, and iii). [b] TOFs are based on the average current density for each sample. The error represents the standard error of results from 2-3 times' measurements. Except at the lowest loading, i.e, 1.0 μg cm^{-2}, the TOFs of samples with different loadings in this range are similar. The TOFs at 1.0 μg cm^{-2} are significantly higher, in agreement with recent observations that at an ultralow loading (≤ 1 μg cm^{-2}) the TOFs of certain OER catalysts were abnormally high compared to the same catalysts at loadings between 1.4 to 14.1 μg cm^{-2}. A "substrate effect"[11] or "nucleus sintering" [12] was invoked to rationalize these observations. The intrinsic activity, however, is best represented by TOFs at higher loadings [12]

Supplementary Table 2. Current densities and TOFs of all Au-NiO_x-Fe electrodes (loading range: 0.98-2.13 μg cm^{-2}) at overpotentials of 250, 270, and 300 mV, respectively.

Au-NiO_x-Fe	Loading (μg cm^{-2})	η@10 mA cm^{-2} (mV)	*J* (mA cm^{-2}) [a]						TOF (s^{-1}) [b]		
			250 mV		270 mV		300 mV		250 mV	270 mV	300 mV
			i	ii	i	ii	i	ii			
1#	0.98	285	1.2	0.95	4.3	3.6	20	16	0.23±0.03	0.84±0.07	3.82±0.42
2#	1.04	282	1.4	1.5	5.7	6.3	28.4	33.5	0.29±0.01	1.19±0.06	6.14±0.51
3#	1.29	290	0.83	1.14	3.2	3.8	15	18	0.16±0.02	0.56±0.05	2.66±0.24
4#	1.55	283	1.4	1.5	5.05	5.9	24	29.5	0.19±0.01	0.73±0.06	3.57±0.37
5#	1.69	283	1.2	1.7	4.85	5.5	23.1	28	0.18±0.03	0.63±0.04	3.13±0.30
6#	2.09	280	1.7	1.2	6	4.2	25.4	18.5	0.14±0.02	0.51±0.09	2.18±0.34
7#	2.13	275	2.1	1.6	8.2	5.9	37	31	0.18±0.02	0.69±0.11	3.31±0.29

[a] Each sample is measured 2 times and the current densities for each measurement are listed (i and ii). [b] TOFs are based on the average current density for each sample. The error represents the standard error of results.

Supplementary Table 3. Current densities and TOFs of all GC-NiO_x-Fe electrodes (loading range: 0.67-1.51 μg cm^{-2}) at overpotentials of 250, 270, and 300 mV, respectively.

GC-NiO_x-Fe	Loading (μg cm^{-2})	η@10 mA cm^{-2} (mV)	*J* (mA cm^{-2}) [a]						TOF (s^{-1}) [b]		
			250 mV		270 mV		300 mV		250 mV	270 mV	300 mV
			i	ii	i	ii	i	ii			
1#	0.67	309	0.362	0.372	1.162	1.32	6.4	6.6	0.12±0.01	0.39±0.02	2.02±0.03
2#	0.80	304	0.458	0.372	1.64	1.402	8.94	8	0.11±0.01	0.40±0.03	2.20±0.12
3#	1.51	287	0.9066	0.94	3.6	3.78	21.2	22	0.13±0.01	0.51±0.01	2.96±0.05
4#	2.11	277	1.91	1.55	7.23	5.66	30.1	25.0	0.16±0.02	0.60±0.10	2.75±0.33

[a] Each sample is measured 2 times and the current densities for each measurement are listed (i and ii). [b] TOFs are based on the average current density for each sample. The error represents the standard error of results.

Supplementary Table 4. Current densities and TOFs of all NF-$NiFeO_x$ and GC-$NiFeO_x$ electrodes (loading range: 1.75-17.30 μg cm^{-2}) at overpotentials of 250, 270, and 300 mV, respectively.

$NiFeO_x$		Loading (μg cm^{-2})	η@10 mA cm^{-2} (mV)	*J* (mA cm^{-2}) [a]						TOF (s^{-1}) [b]		
				250 mV		270 mV		300 mV		250 mV	270 mV	300 mV
				i	ii	i	ii	i	ii			
NF	1#	1.97	338	0.224	0.235	0.65	0.697	3.04	2.73	0.023±0.003	0.062±0.011	0.409±0.072
	2#	5.19	321	0.324	0.321	1.08	1.256	4.59	5.08	0.020±0.001	0.086±0.012	0.348±0.034
	3#	5.54	321	0.325	0.352	0.866	1.00	3.94	4.20	0.020±0.002	0.050±0.009	0.264±0.017
	4#	12.92	323	0.501	0.897	1.02	1.6	3.76	4.65	0.028±0.011	0.042±0.016	0.302±0.024
GC	5#	1.75	360	0.048	0.057	0.128	0.16	0.736	0.894	0.027±0.002	0.075±0.008	0.424±0.041
	6#	7.16	316	0.23	0.32	0.8	1.08	4.514	5.38	0.027±0.004	0.093±0.014	0.489±0.043
	7#	11.97	308	0.558	0.67	1.94	2.22	7.8	8.12	0.036±0.003	0.122±0.008	0.465±0.009
	8#	17.30	304	0.766	0.98	2.516	2.888	8.88	9.22	0.036±0.004	0.111±0.008	0.372±0.007

[a] Each sample is measured 2 times and the current densities for each measurement are listed (i and ii). [b] TOFs are based on the average current density for each sample. The error represents the standard error of results.

Supplementary Table 5. Comparison of TOFs of different OER catalysts in thin film configurations (loading <20 μg cm^{-2}) in alkaline solutions.

Catalysts	TOF (s^{-1}) [a]			Reference
	250 mV	270 mV	300 mV	
NF-AC-NiO_x-Fe	0.24±0.10	0.78±0.27	3.35±1.06	This work
Au-NiOx-Fe	0.20±0.05	0.73±0.23	3.51±1.30	This work
GC-NiOx-Fe	0.13±0.02	0.48±0.10	2.48±0.44	This work
NF-$NiFeO_x$	0.023±0.004	0.06±0.02	0.33±0.06	This work
GC-$NiFeO_x$	0.032±0.005	0.10±0.02	0.44±0.05	This work
$NiFeO_x$	0.02±0.004[d]	0.072±0.02[d]	0.52±0.16	[4]
$FeNiO_x$	0.004±0.003	0.013±0.011	0.11±0.09	[12]
$CoFeO_x$	0.011±0.001	0.047±0.003	0.31±0.02	[12]
$Ni_{0.75}Co_{0.25}O_x$	/	/	0.089±0.013	[34]
FeO_x	/	/	0.0015±0.0009	[34]
NiO_x [e]	/	/	0.17±0.04	[34]
CoO_x	/	/	0.0032±0.0014	[34]
MnO_x	/	/	0.0004±0.0002	[34]
IrO_2	~0.001[d]	~0.002[d]	0.0089±0.005	[34]

[a] For multiple samples, the averaged values with standard deviations are given for TOF. For NF-AC-NiO_x-Fe, Au-NiO_x-Fe, GC-NiO_x-Fe, NF-$NiFeO_x$, and GC-$NiFeO_x$, each sample is measured 2-3 times and the raw data are shown in Supplementary Table S1-S4. For all iron-containing samples, iron is assumed as the active species. For samples without iron, all the other metal elements are assumed as the active species. The current densities are high and partially limited by mass-transport at $\eta \geq 300$ mV, as reflected in the Tafel plots (Supplementary Fig. 3). Thus, the apparent TOFs of NF-AC-NiO_x-Fe at $\eta \geq 300$ mV underestimate its intrinsic activity, and the TOFs at η = 250 and 270 mV are better representatives of the activity of this catalyst. [d] TOFs at these potentials were extrapolated using the reported Tafel slopes (~35 mV dec^{-1} for $NiFeO_x$ and ~40 mV dec^{-1} for IrO_2). [e] NiO_x was likely to contain some Fe incorporated from electrolyte during the OER test.

Supplementary Table 6. Specific current density (J_s) (normalized to the electrochemical surface area) at overpotentials of 250, 270, and 300 mV, respectively.

Samples	J_s (mA cm^{-2}) [a]			reference
	250 mV	270 mV	300 mV	
NF-AC-NiO_x-Fe	0.013±0.005	0.041±0.018	0.18±0.08	This work
NF-AC-FD-NiO_x-Fe	0.019±0.002	0.051±0.008	/	This work
NF -$NiFeO_x$	0.004±0.002	0.012±0.002	0.05±0.01	This work
GC-NiO_x-Fe	0.026±0.007	0.10±0.03	0.54±0.09	This work
GC-$NiFeO_x$	0.008±0.003	0.03±0.01	0.13±0.04	This work
$NiFeO_x$ [b]	0.003 [c]	0.011 [c]	0.084	9
$NiFeO_x$ [b]	0.004±0.003 [c]	0.015±0.010 [c]	0.11±0.07 [c]	10

[a] J_s are based on the average J_s for all samples of the same kind. The error represents the standard deviation of results. [b] The calculation of J_s from the literature is shown in Supplementary Method. [c] J_s at these potentials are extrapolated using the reported Tafel slopes (~35 mV dec^{-1})

Supplementary Table 7. Comparison of η@10 mA cm^{-2} of different OER catalysts in thin film configurations (loading <20 μg cm^{-2}) alkaline solutions.

Catalysts	Loading [b] (μg cm^{-2})	η@10 mA cm^{-2} (mV)	Reference
NF-AC-NiO_x-Fe [a]	1.4-14.1	245-270	This work
Au-NiOx-Fe [a]	0.98-2.13	275-290	This work
GC-NiOx-Fe [a]	0.67-2.11	277-309	This work
NF-$NiFeO_x$ [a]	2.0-12.9	321-338	This work
GC-$NiFeO_x$ [a]	1.75-17.30	304-360	This work
$NiFeO_x$ [a]	1.2-12	~311 [c]	[4]
$FeNiO_x$ [a]	1.3-3.0	370-378	[12]
$CoFeO_x$ [a]	1.9-5.5	333-349	[12]
$Ni_{0.75}Co_{0.25}O_x$	1.04±0.09	445±2	[34]
FeO_x	1.63±0.08	456±7	[34]
NiO_x [d]	1.13±0.10	329±3	[34]
CoO_x	1.32±0.14	423±13	[34]
MnO_x	1.13±0.08	563±25	[34]
IrO_2	4.12±0.14	427±5	[34]

[a] For multiple samples, the value ranges are given for loading and η@10mA cm^{-2}. For NF-AC-NiO_x-Fe, Au-NiO_x-Fe, GC-NiO_x-Fe, NF-$NiFeO_x$, and GC-$NiFeO_x$, the raw data are shown in Supplementary Table S1-S4. [b] The loading is based on the quantity of the active metal species, in the form of metal oxides. [c] Overpotential is for the catalyst at the loading of around 8.3 ug cm^{-2}. [d] NiO_x is likely to contain some Fe that were incorporated from electrolyte in the OER test.

Supplementary Table 8. Comparison of the geometric activity of porous electrodes coated by a high-loading of catalysts in 1M KOH.

Catalysts	**Electrodes** [a]	**Loading (mg cm^{-2})**	***η*@10 mA cm^{-2}** (mV)	***η*@100 mA cm^{-2}** (mV)	**Reference**
NF-AC-FD-NiO_x-Fe	NF	0.068	215	248	This work
$Fe(PO_3)_2/Ni_2P$	NF	8.0 [b]	177 [c]	221	[35]
G-FeCoW	NF(Au coated)	0.4	191±3	/	[26]
Ni_2P-Ni	NF	/	200	268	[36]
EG/$Co_{0.85}Se$/NiFe LDH	Graphene Foam	4.0	203	260	[37]
$Ni_{60}Fe_{30}Mn_{10}$	Alloy Foam	76. 0	208	270	[38]
$NiFeO_x$	CFP	1.6	230	271	[39]
NiFe hydroxides	NF	/	245	280	[40]
NiSe	NF	2.8	251	314	[41]
NiFe LDH	NF	1.0	240-256	∼306	[42,43]
IrO_2	CFP	3.3	264	/	[44,45]

[a] NF: nickel foam; CFP: carbon fiber paper. [b] Loading of $Fe(PO_3)_2$. [c] Overpotential at this current density was extrapolated using the reported Tafel slopes (~52 mV dec^{-1}).

Supplementary Table 9 | Structural parameters of γ–FeOOH, NiFe LDH and NF-AC-NiO_x-Fe samples extracted from EXAFS refinement.

path	R (Å)	CN	ΔE (eV)	σ^2 ($Å^2$)	R-value (%)
γ-FeOOH					
Fe-O	1.99(4)	6.4(3)	-5.9(3)	0.0088(5)	2.035
Fe-Fe	3.08(6)	5.4(5)	-4.3(7)	0.0082(4)	
NiFe LDH					
Fe-O	2.00(1)	5.8(1)	-5.0(6)	0.0071(1)	1.429
Fe-Fe	3.07(1)	3.4(3)	-1.1(9)	0.0085(3)	
Fe-Ni_{Oh}	3.11(2)	2.6(4)	-7.9(8)	0.0055(4)	
NF-AC-NiOx-Fe					
Fe-O	1.98(1)	4.8(2)	1.4(8)	0.0095(2)	0.798
Fe-Fe	3.06(2)	2.3(2)	1.3(6)	0.0071(1)	
Fe-Ni_{Oh}	-	-	-	-	
Fe-$Ni_{outside}$	3.98(4)	3.6(4)	3.2(7)	0.0080(6)	

Supplementary Table 10 | Structural parameters of Au-NiO_x-Fe sample extracted from Ni K-edge EXAFS measured under *ex situ* and *operando* conditions.

condition	path	R (Å)	CN	ΔE (eV)	σ^2 ($Å^2$)	R-value (%)
Dry sample	Ni-O	2.04(4)	6.0(3)	-5.1(5)	0.0076(4)	2.517
	Ni-Ni	3.09(5)	6.1(1)	-1.0(6)	0.0076(3)	
No bias	Ni-O	2.04(4)	6.0(3)	-5.4(5)	0.0081(9)	2.023
	Ni-Ni	3.10(6)	6.1(6)	1.5(7)	0.0071(9)	
η = 0.22	Ni-O	2.04(3)	6.0(1)	-5.6(5)	0.0072(9)	2.386
	Ni-Ni	3.10(5)	6.0(2)	-5.7(7)	0.0068(9)	
η = 0.27	Ni-O	1.86(4)	5.5(1)	-7.2(5)	0.0080(1)	3.170
	Ni-Ni	2.82(6)	5.1(4)	-2.3(9)	0.0076(1)	
η = 0.32	Ni-O	1.88(4)	5.6(2)	-4.9(3)	0.0080(1)	3.209
	Ni-Ni	2.84(4)	5.0(3)	-3.9(6)	0.0064(1)	
η = 0.37	Ni-O	1.89(2)	5.6(2)	-3.6(4)	0.0059(3)	6.667
	Ni-Ni	2.85(3)	5.0(3)	1.8(6)	0.0058(2)	

References and Notes

1 Yeo, B. S. & Bell, A. T. In situ raman study of nickel oxide and gold-supported nickel oxide catalysts for the electrochemical evolution of oxygen. *J. Phys. Chem. C* **116**, 8394-8400 (2012).

2 Fu, X.-Z. *et al.* Nickel oxyhydroxides with various oxidation states prepared by chemical oxidation of spherical β-Ni(OH)2. *Solid State Ionics* **178**, 987-993 (2007).

3 Xu, X., Song, F. & Hu, X. A nickel iron diselenide-derived efficient oxygen-evolution catalyst. *Nat. Commun.* **7**, 12324 (2016).

4 Trotochaud, L., Young, S. L., Ranney, J. K. & Boettcher, S. W. Nickel-iron oxyhydroxide oxygen-evolution electrocatalysts: The role of intentional and incidental Iron incorporation. *J. Am. Chem. Soc.* **136**, 6744-6753 (2014).

5 Burke, M. S. *et al.* Revised oxygen evolution reaction activity trends for first-row transition-metal (oxy)hydroxides in alkaline media. *J. Phys. Chem. Lett.* **6**, 3737-3742 (2015).

6 de Faria, D. L. A., Venâncio Silva, S. & de Oliveira, M. T. Raman microspectroscopy of some iron oxides and oxyhydroxides. *J. Raman Spectrosc.* **28**, 873-878 (1997).

7 Gregoire, B., Ruby, C. & Carteret, C. Hydrolysis of mixed Ni^{2+}-Fe^{3+} and Mg^{2+}-Fe^{3+} solutions and mechanism of formation of layered double hydroxides. *Dalton Trans.* **42**, 15687-15698 (2013).

8 Chakthranont, P. *et al.* Effects of gold substrates on the intrinsic and extrinsic activity of high-loading nickel-based oxyhydroxide oxygen evolution catalysts. *Acs Catal.* **7**, 5399-5409 (2017).

9 Batchellor, A. S. & Boettcher, S. W. Pulse-electrodeposited Ni-Fe (oxy)hydroxide oxygen evolution electrocatalysts with high geometric and intrinsic activities at large mass loadings. *Acs Catal.* **5**, 6680-6689 (2015).

10 McCrory, C. C. L., Jung, S. H., Peters, J. C. & Jaramillo, T. F. Benchmarking heterogeneous electrocatalysts for the oxygen evolution reaction. *J. Am. Chem. Soc.* **135**, 16977-16987 (2013).

11 Yeo, B. S. & Bell, A. T. Enhanced activity of gold-supported cobalt oxide for the electrochemical evolution of oxygen. *J. Am. Chem. Soc.* **133**, 5587-5593 (2011).

12 Morales-Guio, C. G., Liardet, L. & Hu, X. Oxidatively electrodeposited thin-film transition metal (oxy)hydroxides as oxygen evolution catalysts. *J. Am. Chem. Soc.* **138**, 8946-8957 (2016).

13 Vantelon, D. *et al.* The LUCIA beamline at SOLEIL. *J. Synchrotron Radiat.* **23**, 635-640 (2016).

14 Rehr, J. J. & Albers, R. C. Theoretical approaches to x-ray absorption fine structure. *Rev. Mod. Phys.* **72**, 621-654 (2000).

15 Newville, M. EXAFS analysis using FEFF and FEFFIT. *J. Synchrotron Radiat.* **8**, 96-100 (2001).

16 Mortensen, J. J., Hansen, L. B. & Jacobsen, K. W. Real-space grid implementation of the projector augmented wave method. *Phys. Rev. B* **71**, 035109 (2005).

17 Enkovaara, J. *et al.* Electronic structure calculations with GPAW: a real-space implementation of the projector augmented-wave method. *J. Phys.: Condens. Matter* **22**, 253202 (2010).

18 Hammer, B., Hansen, L. B. & Nørskov, J. K. Improved adsorption energetics within density-functional theory using revised Perdew-Burke-Ernzerhof functionals. *Phys. Rev. B Condens. Matter* **59**, 7413-7421 (1999).

19 Blöchl, P. E. Projector augmented-wave method. *Phys. Rev. B* **50**, 17953-17979 (1994).

20 Busch, M., Ahlberg, E. & Panas, I. Validation of binuclear descriptor for mixed transition metal oxide supported electrocatalytic water oxidation. *Catal. Today* **202**, 114-119 (2013).

21 Busch, M., Ahlberg, E. & Panas, I. Hydroxide oxidation and peroxide formation at embedded binuclear transition metal sites; TM = Cr, Mn, Fe, Co. *Phys. Chem. Chem. Phys.* **13**, 15062-15068 (2011).

22 Rossmeisl, J., Logadottir, A. & Norskov, J. K. Electrolysis of water on (oxidized) metal surfaces. *Chem. Phys.* **319**, 178-184 (2005).

23 Su, H.-Y. *et al.* Identifying active surface phases for metal oxide electrocatalysts: a study of manganese oxide bi-functional catalysts for oxygen reduction and water oxidation catalysis. *Phys. Chem. Chem. Phys.* **14**, 14010-14022 (2012).

24 Diaz-Morales, O., Ledezma-Yanez, I., Koper, M. T. M. & Calle-Vallejo, F. Guidelines for the rational design of Ni-based double hydroxide electrocatalysts for the oxygen evolution reaction. *ACS Catal.* **5**, 5380-5387 (2015).
25 Man, I. C. *et al.* Universality in oxygen evolution electrocatalysis on oxide surfaces. *ChemCatChem* **3**, 1159-1165 (2011).
26 Zhang, B. *et al.* Homogeneously dispersed multimetal oxygen-evolving catalysts. *Science* **352**, 333-337 (2016).
27 Frydendal, R. *et al.* Enhancing activity for the oxygen evolution reaction: the beneficial interaction of gold with manganese and cobalt oxides. *ChemCatChem* **7**, 149-154 (2015).
28 Bajdich, M., Garcia-Mota, M., Vojvodic, A., Norskov, J. K. & Bell, A. T. Theoretical investigation of the activity of cobalt oxides for the electrochemical oxidation of water. *J. Am. Chem. Soc.* **135**, 13521-13530 (2013).
29 Busch, M. *et al.* Beyond the top of the volcano? – A unified approach to electrocatalytic oxygen reduction and oxygen evolution. *Nano Energy* **29**, 126-135 (2016).
30 Yin, L. I., Yellin, E. & Adler, I. X-Ray excited LMM auger spectra of copper, nickel, and iron. *J. Appl. Phys.* **42**, 3595-3600 (1971).
31 Louie, M. W. & Bell, A. T. An investigation of thin-film Ni–Fe oxide catalysts for the electrochemical evolution of oxygen. *J. Am. Chem. Soc.* **135**, 12329-12337 (2013).
32 Biesinger, M. C. *et al.* Resolving surface chemical states in XPS analysis of first row transition metals, oxides and hydroxides: Cr, Mn, Fe, Co and Ni. *Appl. Surf. Sci.* **257**, 2717-2730 (2011).
33 Grosvenor, A. P., Kobe, B. A., Biesinger, M. C. & McIntyre, N. S. Investigation of multiplet splitting of Fe 2p XPS spectra and bonding in iron compounds. *Surf. Interface Anal.* **36**, 1564-1574 (2004).
34 Trotochaud, L., Ranney, J. K., Williams, K. N. & Boettcher, S. W. Solution-cast metal oxide thin film electrocatalysts for oxygen evolution. *J. Am. Chem. Soc.* **134**, 17253-17261 (2012).
35 Zhou, H. Q. *et al.* Highly active catalyst derived from a 3D foam of $Fe(PO_3)_2/Ni_2P$ for extremely efficient water oxidation. *Proc. Natl. Acad. Sci. USA* **114**, 5607-5611 (2017).
36 You, B., Jiang, N., Sheng, M. L., Bhushan, M. W. & Sun, Y. J. Hierarchically porous urchin-like Ni_2P superstructures supported on nickel foam as efficient bifunctional electrocatalysts for overall water splitting. *Acs Catal.* **6**, 714-721 (2016).
37 Hou, Y. *et al.* Vertically oriented cobalt selenide/NiFe layered-double-hydroxide nanosheets supported on exfoliated graphene foil: an efficient 3D electrode for overall water splitting. *Energ. Environ.l Sci.* **9**, 478-483 (2016).
38 Detsi, E. *et al.* Mesoporous $Ni_{60}Fe_{30}Mn_{10}$-alloy based metal/metal oxide composite thick films as highly active and robust oxygen evolution catalysts. *Energ. Environ.l Sci.* **9**, 540-549 (2016).
39 Wang, H. T. *et al.* Bifunctional non-noble metal oxide nanoparticle electrocatalysts through lithium-induced conversion for overall water splitting. *Nat. Commun.* **6**, 7261 (2015).
40 Lu, X. Y. & Zhao, C. A. Electrodeposition of hierarchically structured three-dimensional nickel-iron electrodes for efficient oxygen evolution at high current densities. *Nat. Commun.* **6**, 6616 (2015).
41 Tang, C., Cheng, N., Pu, Z., Xing, W. & Sun, X. NiSe nanowire film supported on nickel foam: an efficient and stable 3D bifunctional electrode for full water splitting. *Angew. Chem. Int. Ed.* **54**, 9351-9355 (2015).
42 Lu, Z. *et al.* Three-dimensional NiFe layered double hydroxide film for high-efficiency oxygen evolution reaction. *Chem. Commun.* **50**, 6479-6482 (2014).
43 Luo, J. S. *et al.* Water photolysis at 12.3% efficiency via perovskite photovoltaics and Earth-abundant catalysts. *Science* **345**, 1593-1596 (2014).
44 Yan, X. D. *et al.* From Water oxidation to reduction: transformation from $Ni_xCo_{3-x}O_4$ nanowires to $NiCo/NiCoO_x$ heterostructures. *Acs Appl. Mater. Interfaces* **8**, 3208-3214 (2016).

45 Wang, P., Song, F., Amal, R., Ng, Y. H. & Hu, X. Efficient water splitting catalyzed by cobalt phosphide-based nanoneedle arrays supported on carbon cloth. *ChemSusChem* **9**, 472-477 (2016).

DFT Structures

γ-FeOOH (010) – Fe bare

Cell:

25.0000000000000000 0.0000000000000000 0.0000000000000000 -
3.1524999999999999 5.4602851999999995 0.0000000000000000
0.0000000000000000 -0.0000000000000000 10.0000000000000000

xyz coordinates

O	5.67344417	1.30902184	3.94323191
O	4.09719417	4.03916444	3.94323191
O	8.82594417	1.30902184	3.94323191
O	7.24969417	4.03916444	3.94323191
O	11.97844417	1.30902184	3.94323191
O	10.40219417	4.03916444	3.94323191
O	15.17307106	1.45864325	3.91920680
O	13.68149577	4.00907130	3.92803847
O	17.81995030	1.09068833	3.65023839
O	7.25610552	2.21574101	6.00454361
O	5.67985552	4.94588361	6.00454361
O	10.40860552	2.21574101	6.00454361
O	8.83235552	4.94588361	6.00454361
O	13.50860992	2.18274513	6.06554899
O	12.07800776	5.00972327	5.82538241
O	16.67367052	2.14796858	6.04065515
O	15.12133226	4.91031827	5.92254901
Fe	7.25384250	0.39563374	5.12304955
Fe	5.67759250	3.12577634	5.12304955
Fe	10.40634250	0.39563374	5.12304955
Fe	8.83009250	3.12577634	5.12304955
Fe	13.53896568	0.36290398	5.20953084
Fe	11.94959123	3.14078623	5.21673059
Fe	16.78322813	0.44009994	4.79266526
Fe	15.05880971	3.05232639	5.31171158
H	8.83976609	1.30304303	2.96881635
H	7.26351609	4.03318563	2.96881635
H	11.99226609	1.30304303	2.96881635
H	10.41601609	4.03318563	2.96881635
H	15.39095324	1.65072463	2.99186186
H	13.93602091	4.06492206	2.99245410
H	15.37302592	5.17766082	6.82055985
H	16.60056161	1.92167597	6.98352733

γ-FeOOH (010) – Fe-OH

Cell:

25.0000000000000000 0.0000000000000000 0.0000000000000000 -3.1524999999999999 5.4602851999999995 0.0000000000000000
0.0000000000000000 -0.0000000000000000 10.0000000000000000

xyz coordinates

O	5.36816161	1.35136899	3.98052770
O	3.79191161	4.08151159	3.98052770
O	8.52066161	1.35136899	3.98052770
O	6.94441161	4.08151159	3.98052770
O	11.67316161	1.35136899	3.98052770
O	10.09691161	4.08151159	3.98052770
O	14.79150953	1.17044360	3.87039109
O	13.31166528	3.96332554	3.87024155
O	17.49656795	1.22171150	3.89884562
O	16.04124007	3.81833988	3.87285374
O	6.95082297	2.25808815	6.04183940
O	5.37457297	4.98823075	6.04183940
O	10.10332297	2.25808815	6.04183940
O	8.52707297	4.98823075	6.04183940
O	13.31527348	2.32200284	5.93071330
O	11.71003906	5.01383284	5.93156759
O	16.03107459	2.27346355	6.11453774
O	14.50480999	5.02744240	6.09527404
Fe	6.94855994	0.43798089	5.1603453
Fe	5.37230994	3.16812349	5.1603453
Fe	10.10105994	0.43798089	5.1603453
Fe	8.52480994	3.16812349	5.1603453
Fe	13.23350086	0.43476777	5.2140221
Fe	11.63805066	3.18048559	5.2271521
Fe	16.37250049	0.49849419	4.9153296
Fe	14.77403854	3.23388839	5.0281536
H	8.53448353	1.34539018	3.00611213
H	6.95823353	4.07553278	3.00611213
H	11.68698353	1.34539018	3.00611213
H	10.11073353	4.07553278	3.00611213
H	14.97960021	1.38450560	2.94210460
H	13.61900321	4.11913077	2.95994111
H	16.82518154	3.22270614	3.87908090
H	13.99741684	4.80382083	6.89819126
H	15.55266149	2.00536458	6.92258046

γ-FeOOH (010) – Fe=O

Cell:

25.0000000000000000 0.0000000000000000 0.0000000000000000 -3.1524999999999999 5.4602851999999995 0.0000000000000000
0.0000000000000000 -0.0000000000000000 10.0000000000000000

xyz coordinates

O	5.68684391	1.34165963	4.04134256
O	4.11059391	4.07180223	4.04134256
O	8.83934391	1.34165963	4.04134256
O	7.26309391	4.07180223	4.04134256
O	11.99184391	1.34165963	4.04134256
O	10.41559391	4.07180223	4.04134256
O	15.11709353	1.35754201	3.99105782
O	13.53971957	4.09613414	3.98691172
O	17.87330828	1.13586189	4.04405427
O	16.30002307	3.85351788	4.04164799
O	7.26950527	2.24837879	6.10265426
O	5.69325527	4.97852139	6.10265426
O	10.42200527	2.24837879	6.10265426
O	8.84575527	4.97852139	6.10265426
O	13.58199497	2.28692099	6.01894533
O	12.00512062	5.01586984	6.01892834
O	16.42589402	2.11463257	6.18913178
O	14.83898906	4.85937360	6.18406665
Fe	7.26724224	0.42827153	5.2211602
Fe	5.69099224	3.15841413	5.2211602
Fe	10.41974224	0.42827153	5.2211602
Fe	8.84349224	3.15841413	5.2211602
Fe	13.55229131	0.44881578	5.3056220
Fe	11.97649848	3.17910472	5.3040863
Fe	16.72919895	0.47416677	5.0544928
Fe	15.15513982	3.20235933	5.0578390
H	8.85316583	1.33568082	3.06692699
H	7.27691583	4.06582342	3.06692699
H	12.00566583	1.33568082	3.06692699
H	10.42941583	4.06582342	3.06692699
H	15.36286868	1.50413367	3.06163934
H	13.79396391	4.23931386	3.05861229
H	14.31486070	4.57540816	6.95842705
H	15.90560465	1.82153153	6.96340730

γ-FeOOH (010) – Fe-OOH

Cell:

25.0000000000000000 0.0000000000000000 0.0000000000000000 -3.1524999999999999 5.4602851999999995 0.0000000000000000
0.0000000000000000 -0.0000000000000000 10.0000000000000000

xyz coordinates

O	4.97425609	1.34326757	4.04114476
O	3.39800609	4.07341017	4.04114476
O	8.12675609	1.34326757	4.04114476
O	6.55050609	4.07341017	4.04114476
O	11.27925609	1.34326757	4.04114476
O	9.70300609	4.07341017	4.04114476
O	14.37494270	1.31239559	3.95782111
O	12.88601822	4.08959427	3.95478847
O	17.13540627	1.25212825	4.02535647
O	15.67720214	3.93856184	3.98408227
O	6.55691744	2.24998673	6.10245646
O	4.98066744	4.98012933	6.10245646
O	9.70941744	2.24998673	6.10245646
O	8.13316744	4.98012933	6.10245646
O	12.87579835	2.31089178	6.01778529
O	11.31671405	5.03858553	5.97651478
O	15.68809582	2.15375160	6.22055239
O	14.13492143	4.94307047	6.21630742
O	17.01743116	3.83153828	4.29546924
Fe	6.55465441	0.42987947	5.2209624
Fe	4.97840441	3.16002207	5.2209624
Fe	9.70715441	0.42987947	5.2209624
Fe	8.13090441	3.16002207	5.2209624
Fe	12.82772607	0.45055589	5.2736390
Fe	11.24548236	3.18605996	5.2866508
Fe	15.98545165	0.49671911	5.0122754
Fe	14.40137119	3.22905970	5.1504895
H	8.14057801	1.33728876	3.06672919
H	6.56432801	4.06743136	3.06672919
H	11.29307801	1.33728876	3.06672919
H	9.71682801	4.06743136	3.06672919
H	14.55048860	1.45033766	3.01185629
H	13.11588939	4.21733248	3.01858501
H	13.64253510	4.69781545	7.02253764
H	15.23597810	1.83582836	7.02477490
H	17.20530071	2.82580563	4.15689959

γ-$Ni(OH)_2$ (0001) – reduced

Cell:

6.535012 0.0 0.0
-3.267506 5.6594901 0.0
0.0 0.0 12.0

xyz-coordinates

O	1.90311068	1.41387317	5.00563898
H	1.86929724	1.41709539	4.03660623
Ni	0.27517317	0.47174663	5.99909845
O	0.28113025	2.35770323	6.99385990
H	0.29466067	2.32533586	7.96317989
O	0.26935913	4.24361866	5.00563819
H	0.23554433	4.24683978	4.03660658
Ni	-1.35857973	3.30148646	5.99909642
O	-1.35262429	5.18744783	6.99386051
H	-1.33909241	5.15508162	7.96317950
O	5.17061670	1.41387146	5.00563836
H	5.13680387	1.41709566	4.03660661
Ni	3.54267462	0.47174416	5.99910022
O	3.54863603	2.35770490	6.99386049
H	3.56216605	2.32533563	7.96317953
O	3.53686615	4.24361635	5.00563620
H	3.50305099	4.24684001	4.03660632
Ni	1.90892188	3.30148425	5.99909835
O	1.91488068	5.18745005	6.99386258
H	1.92841295	5.15508138	7.96317976

γ-$Ni(OH)_2$ (0001) – oxidised

Cell:

6.535012 0.0 0.0
-3.267506 5.6594901 0.0
0.0 0.0 12.0

xyz-coordinates

O	1.90718120	1.41024989	5.11026479
Ni	0.33748037	0.50393985	5.97035697
O	0.26348653	2.36150202	7.00954288
H	0.28606505	2.34548947	7.97964602
O	0.25860079	4.23283676	5.01888013
H	0.24039563	4.23769611	4.04831928
Ni	-1.36355305	3.29546123	5.99983967
O	-1.35787566	5.17103119	7.01106629
H	-1.34931908	5.16992087	7.98178655
O	5.16590280	1.41902658	5.02110175
H	5.15659766	1.43180123	4.05041585
Ni	3.47666637	0.50131379	5.97375789
O	3.55851614	2.35766582	7.01412879
H	3.55697017	2.34679260	7.98470186
O	3.54206516	4.22879661	5.02092673
H	3.54183501	4.23319442	4.05010419
Ni	1.90588953	3.22201426	5.97196221
O	1.90368936	5.18413400	6.88979005
H	1.91840602	5.17262113	7.86117393

γ-NiOOH (0001) – reduced

Cell:

6.065992 0.0 0.0
-3.032996 5.2533066 0.0
0.0 0.0 12.0

xyz-coordinates

O	1.71076370	1.37210496	5.12338706
H	1.67051527	1.39634735	4.15397780
Ni	0.24651552	0.40393467	6.09946491
O	0.25310378	2.21142319	7.17283136
O	0.23973986	3.90597127	5.11644904
H	0.22674532	3.88691776	4.14504379
Ni	-1.32507587	3.12385221	6.11129305
O	-1.37471864	4.78586672	7.02319678
O	4.84473557	1.37876029	5.11451478
H	4.85685689	1.40390616	4.14333712
Ni	3.27964809	0.46507507	6.23967882
O	3.27819645	2.33558727	7.03030733
O	3.27787642	3.96663891	4.79139616
H	3.27070267	3.96752005	3.81960624
Ni	1.81627940	3.12255385	6.10517930
O	1.86797982	4.78434828	7.02027213
H	0.27216915	2.19515695	8.14516930

γ-NiOOH (0001) – oxidised

Cell:

6.065992 0.0 0.0
-3.032996 5.2533066 0.0
0.0 0.0 12.0

xyz-coordinates

O	1.76196071	1.31466392	5.49761057
H	1.78588649	1.31192120	4.52501691
Ni	0.23609752	0.43894696	6.59242780
O	0.23380086	2.18777053	7.47429891
O	0.24546274	3.94131647	5.49761025
H	0.26938845	3.93857447	4.52501684
Ni	-1.28040025	3.06559847	6.59242849
O	-1.28269708	4.81442312	7.47430009
O	4.79495781	1.31466454	5.49761031
H	4.81888270	1.31192136	4.52501681
Ni	3.26909197	0.43894607	6.59242718
O	3.26679856	2.18777145	7.47430032
O	3.27845925	3.94131743	5.49760996
H	3.30238472	3.93857460	4.52501674
Ni	1.75259393	3.06559775	6.59242803
O	1.75030098	4.81442378	7.47430146